Microphysical Characteristics of Overshooting Convection from Polarimetric Radar Observations

CAMERON R. HOMEYER

National Center for Atmospheric Research,* Boulder, Colorado, and School of Meteorology, University of Oklahoma, Norman, Oklahoma

MATTHEW R. KUMJIAN

National Center for Atmospheric Research,* Boulder, Colorado, and Department of Meteorology, The Pennsylvania State University, University Park, Pennsylvania

(Manuscript received 5 December 2013, in final form 3 October 2014)

ABSTRACT

The authors present observations of the microphysical characteristics of deep convection that overshoots the altitude of the extratropical tropopause from analysis of the polarimetric radar variables of radar reflectivity factor at horizontal polarization Z_H, differential reflectivity Z_{DR}, and specific differential phase K_{DP}. Identified overshooting convective storms are separated by their organization and intensity into three classifications: organized convection, discrete ordinary convection, and discrete supercell convection. Composite analysis of identified storms for each classification reveals microphysical features similar to those found in previous studies of deep convection, with deep columns of highly positive Z_{DR} and K_{DP} representing lofting of liquid hydrometeors within the convective updraft and above the melting level. In addition, organized and discrete supercell classifications show distinct near-zero Z_{DR} minima aligned horizontally with and at altitudes higher than the updraft column features, likely indicative of the frequent presence of large hail in each case. Composites for organized convective systems show a similar Z_{DR} minimum throughout the portion of the convective core that is overshooting the tropopause, corresponding to Z_H in the range of 15–30 dBZ and negative K_{DP} observations, in agreement with the scattering properties of small hail and/or lump or conical graupel. Additional analyses of the evolution of overshooting storms reveals that the Z_{DR} minima indicative of hail in the middle and upper troposphere and graupel in the overshooting top are associated with the mature and decaying stages of overshooting, respectively, supporting their inferred contributions to the observed polarimetric fields.

1. Introduction

Overshooting convective storms contain strong upward motion capable of deep, rapid vertical transport of air from the lower troposphere to the stratosphere and above the level of neutral buoyancy. Irreversible transport across the tropopause from gravity wave breaking and/or turbulent mixing atop these storms can have significant impacts on chemistry and climate. In particular, transport of cloud ice and water vapor (a greenhouse gas) above the extratropical tropopause has direct impacts on the radiation budget and the rate of global climate change (e.g., Forster and Shine 1999; Solomon et al. 2010). In addition to these direct impacts from water vapor, Anderson et al. (2012) have recently argued that conversion of inorganic chlorine to free radical form as a result of increased stratospheric water vapor will lead to ozone destruction in the lower stratosphere and, consequently, increased human exposure to harmful ultraviolet radiation at the surface. If the frequency of overshooting convection were to increase in a warming climate, the impacts to human health and additional warming of the climate from stratospheric ozone loss and elevated water vapor would be significant. Despite this potentially

significant role of overshooting extratropical convection in the climate system, little is known about the frequency, global distribution, and physical and chemical characteristics of these storms. Developing an understanding of the characteristics of overshooting convection and its role in climate is critical for advancing our understanding of chemistry–climate interactions, since these processes are not resolved in current global climate models.

Because overshooting convective storms are often very deep and provide ample sources of turbulence, direct observations of injected air in the lower stratosphere are limited, and no observations exist within the overshooting top (e.g., Fischer et al. 2003; Hegglin et al. 2004; Homeyer et al. 2014b). There is sufficient residual evidence, however, that convective transport of water vapor into the lower stratosphere is common and can reach altitudes up to 5 km above the tropopause (e.g., Dessler and Sherwood 2004; Ray et al. 2004; Hanisco et al. 2007; Anderson et al. 2012). Cirrus cloud plumes above the anvils of tropopause-penetrating convection also provide visual evidence of these transport processes (e.g., Fujita 1982; Adler et al. 1983; Setvák and Doswell 1991; Levizzani and Setvák 1996). Because of the practical limitations associated with direct measurements in these storms, a commonly used alternative for analysis of the dynamics and chemistry of convective transport is explicit simulation with a numerical model (e.g., Wang 2003; Mullendore et al. 2005; Lane and Sharman 2006; Luderer et al. 2007; Homeyer et al. 2014a). A collective result of these modeling studies is the identification of gravity wave breaking as a primary mechanism for the injection of water vapor into the lower stratosphere, often occurring on the downstream edge of the overshooting top and extending into the downstream anvil region. One additional possibility for convective injection of water vapor is from turbulent mixing and advection downstream of the apex of the overshooting cloud top, which may require unique stability environments in the lower stratosphere (e.g., Wang 2003; Homeyer et al. 2014a).

In addition to the climate impacts associated with overshooting convection, these storms have been shown to be associated with hazardous weather at the surface, such as flooding, hail, tornadoes, and damaging winds, and identification of overshooting tops as a predictor for severe weather has been explored (e.g., Negri 1982; McCann 1983; Brunner et al. 2007; Setvák et al. 2010; Bedka 2011; Dworak et al. 2012). Furthermore, gravity wave generation, breaking, and induced turbulence near the tropopause from overshooting convection are major concerns for aircraft safety and flight planning (e.g., Lane et al. 2003; Lane and Sharman 2006; Bedka et al. 2010). Motivated primarily by these relationships with severe weather and turbulence, several studies have examined methods for the objective identification of overshooting convection from satellite observations of cloud-top radiances and temperature (e.g., Schmetz et al. 1997; Bedka et al. 2010, 2012). One major limitation of these approaches, however, is that the altitude corresponding to the observed cloud-top temperature is inferred using temperature profiles from large-scale meteorological analyses, which do not resolve the diabatic processes associated with individual convective storms and the resultant thermodynamical modification of the tropopause region. Recent attention has also been directed toward space-borne lidar and radar observations of the cloud top, which provide true measurements of the altitude of deep convection (e.g., Setvák et al. 2013). Despite the ability of accurate altitude measurements from these measurement platforms, the spatial and temporal coverage is limited and does not allow for accurate characterization of the frequency, depth, and life cycle of overshooting storms.

Perhaps one of the least understood characteristics of overshooting convection is the microphysical composition and vertical structure, since aircraft measurements in mature convection are often limited to distances more than 30 km from a convective core. Despite the lack of observations near the convective core and within the overshooting top of a convective storm, there are multiple observations revealing the microphysical characteristics at the top of the downstream anvil of continental midlatitude convection, which show predominately large concentrations of frozen drops and chainlike aggregates (e.g., Connolly et al. 2005; Gayet et al. 2012; Stith et al. 2014). Developing an understanding of the microphysical characteristics throughout the horizontal and vertical extent of overshooting convection may shed light on the efficiency of water vapor transport into the lower stratosphere in these storms. In particular, since direct mixing of the overshooting top would likely involve convectively lofted hydrometeors with larger terminal velocities than cloud particles in the downstream anvil, increases in stratospheric water vapor may not be equivalent between the identified injection mechanisms.

An understanding of the microphysical characteristics in these storms could also lead to an improvement in the treatment of hydrometeor growth processes in numerical models. For example, the presence of frozen drops, snow aggregates, or rimed particles each reflect different microphysical processes occurring in deep convection. Determining the distribution of these hydrometeor types in the upper levels of overshooting convection sheds light on the dominant processes responsible for hydrometeor growth. These processes have important links to storm kinematics and thermodynamics via latent heating and thus should be accurately depicted in

parameterization schemes. Additionally, because most bulk microphysics parameterizations employ a limited number of hydrometeor classes, using observations to identify general scattering properties of deep convection may help in making appropriate choices in such parameterizations.

In this study, we provide the first characterizations of the microphysical structure and composition of overshooting convection from dual-polarization S-band (10-cm wavelength) radar observations obtained from the Next Generation Weather Radar (NEXRAD) program Weather Surveillance Radar-1988 Doppler (WSR-88D) operational network in the continental United States (Crum and Alberty 1993). Unlike alternative measurement platforms outlined above, these ground-based polarimetric radar observations allow for characterizations of the microphysical characteristics throughout overshooting convection that are not limited in space or time. To examine these characteristics at high horizontal and vertical resolution, we introduce methods for combination of the polarimetric radar variables from individual radars into three-dimensional composites that build upon the previous work of Homeyer (2014). In the following pages, section 2 describes the radar data and methods used, section 3 reviews the identification of overshooting convection and analysis techniques, and section 4 presents results of the radar analysis and discusses the microphysical interpretation of the observed polarimetric fields.

2. Radar data

a. Observational strategy and the polarimetric variables

Three-dimensional data from NEXRAD WSR-88Ds during March–June 2013 are provided by the National Climatic Data Center (NCDC) on native spherical grids. Figure 1 shows the analysis domain in this study and the International Civil Aviation Organization (ICAO) station identifiers and locations of the radar systems used. For deep convection, scans are completed at 14 elevations in the vertical with the typical time between volume scans of 4–7 min. Data for all radars used in this study are available at a resolution of 0.5° in azimuth and 0.25 km in range for the lowest 3–4 elevations and at 1.0° in azimuth for the remaining elevations. In addition to observations of the radar reflectivity factor at horizontal polarization Z_H and radial Doppler velocity V_R present in the entire NEXRAD record, recent upgrades to the WSR-88D systems for dual-polarization of the radar beam beginning in late 2011 allow for observation of the polarimetric fields of the differential radar reflectivity factor Z_{DR}, differential phase ϕ_{DP}, and the copolar correlation coefficient ρ_{HV}. Rather than direct analysis
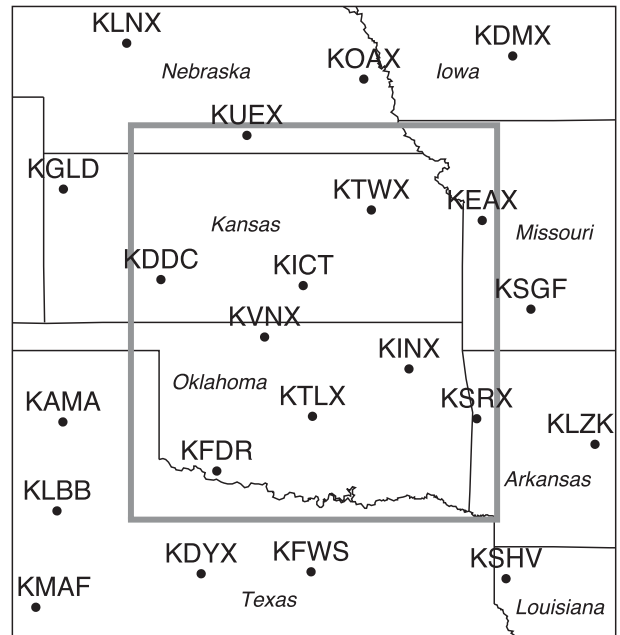

FIG. 1. The region used for characterization of overshooting storms in this study (gray outline) and ICAO station identifiers and locations (black dots) of contributing NEXRAD WSR-88Ds.

of ϕ_{DP}, we compute half the range derivative of ϕ_{DP} (the specific differential phase, or K_{DP}), and retain Z_H, Z_{DR}, and K_{DP} for analysis of overshooting convection.

The three variables used in this study provide information on the characteristics of anisotropic particles that can be used to classify their distributions in an observed storm. The variable used most often for determining hydrometeor size is Z_H, since the majority of detectable hydrometeors at S band are observed with their major axis oriented in the horizontal dimension. Because Z_H is proportional to the sixth moment of the observed particle size distribution (i.e., $Z \sim D^6$, where D is the mean diameter of particles within a volume), the magnitude of Z_H is largely sensitive to particle size. The shape of hydrometeors can be determined from both Z_{DR} and K_{DP} observations, and contrasting the two fields can be beneficial for microphysical identification. In particular, since Z_{DR} is a radar reflectivity (or size) weighted observation of particle shape, its value typically represents the shape of the largest hydrometeors in an observed volume. Alternatively, K_{DP} observations typically represent the concentration of nonspherical particles in a volume, as it is not affected by spherical particles. One important limitation of K_{DP}, however, is that instantaneous observations can suffer from a considerable amount of random noise, particularly in light rain or ice. Despite this limitation, recent studies have shown that time and space averaging of K_{DP} largely

removes this noise and provides some of the most accurate radar-derived estimations of precipitation (e.g., Ryzhkov et al. 2005b; Borowska et al. 2011). Additional detailed descriptions of the polarimetric variables and their physical meaning can be found in several textbooks (e.g., Doviak and Zrnić 1993; Bringi and Chandrasekar 2001) and review papers (e.g., Herzegh and Jameson 1992; Hubbert et al. 1998; Zrnić and Ryzhkov 1999; Straka et al. 2000; Ryzhkov et al. 2005c; Kumjian 2013a,b,c).

One particularly useful characteristic routinely identified in both Z_{DR} and K_{DP} observations of convection that we will refer to repeatedly in this study coincides with the updraft location. In particular, highly positive columns of Z_{DR} and K_{DP} extending to altitudes above the melting level (0°C, typically located between 3 and 5 km in altitude for the study region) represent deep lofting of supercooled liquid and rain droplets within the convective updraft [e.g., see Kumjian et al. (2014) and references therein].

b. Challenges: Bias correction and artifacts

A primary challenge to analyzing polarimetric radar observations from several radars is correcting data for common sources of error. Errors in the polarimetric fields can occur randomly (i.e., noise), systematically from poor radar calibration, and observationally in conjunction with unique hydrometeor distributions aligned in range from the radar. These error sources primarily impact observations of Z_{DR}, since errors in Z_H or Z_V that are generally insignificant for particle size determination can characteristically change the identification of particle shape. Although random error is common in observations of K_{DP}, this polarimetric field is not affected by calibration, and biases from observational error sources are often insignificant. In this study, we correct only for systematic biases in Z_{DR}. An outline of common observational sources of error and justification for neglecting them in our composite analysis is given below within this section.

Systematic biases in Z_{DR} observations from WSR-88D systems have recently been shown to be common and can change in both magnitude and sign between rain events (e.g., Cunningham et al. 2013). In addition, Cunningham et al. (2013) have found that both maintenance and calibration cycles for WSR-88D systems are directly associated with large changes in systematic biases over time. These biases can introduce unphysical variations in the three-dimensional composite fields that may affect the microphysical interpretation of overshooting storms. Melnikov et al. (2003) describe the steps required for calibration of Z_{DR} on the research polarimetric WSR-88D system at Norman, Oklahoma (KOUN). Briefly, one must account for potential biases

introduced in the receiving chain by differences in the relative gain at H and V polarizations, at the transmitter owing to different transmit powers at H and V polarizations, and owing to differences in the noise powers at H and V polarizations. In addition, solar scans can be used to provide an estimate of biases introduced by the antenna and feed (Melnikov et al. 2013b). This so-called "engineering method" for system Z_{DR} calibration works well for research radars when the operator has full control over all components. It has been implemented on the entire network of polarimetric WSR-88Ds, but with limited success (e.g., Melnikov et al. 2013b; Cunningham et al. 2013).

Because of the unavailability of information needed to apply the engineering method to publicly available WSR-88D data in the NCDC archive, alternative methods for Z_{DR} bias correction are required. Methods such as the cross-polar power technique (Hubbert et al. 2003), and use of "natural scatterers," such as snow aggregates (Ryzhkov et al. 2005a), light rain (A. Ryzhkov, 2013, personal communication), and Bragg scatter (Melnikov et al. 2011, 2013a) are being pursued currently. In this study, we correct for Z_{DR} biases using a novel natural scatterer approach, where relationships between Z_{DR} and Z_H for Z_H ranging from 20 to 30 dBZ are contrasted with expected relationships in high-altitude anvil regions composed primarily of snow aggregates [similar in principle to those in Ryzhkov et al. (2005a)]. In particular, Z_{DR} corresponding to snow aggregates in the high-altitude anvil in each observation is compared to expected values in order to determine biases. For example, if Z_{DR} observations in the anvil region from a given radar system are routinely higher (lower) than expected during an hour of continuous observation (about 12 volume scans), we correct the full three-dimensional Z_{DR} field prior to compositing by subtracting (adding) the value of the observed offset. Anvil regions are identified in each volume following methods similar to those in Feng et al. (2011), where an observation is classified as anvil where Z_H is present only at upper levels in a column and only those points above the melting level (where snow aggregates are possible) are used to estimate bias.

To establish the expected relationship between Z_{DR} and Z_H for bias correction, we use data from KOUN that have undergone conventional calibration techniques (the engineering method) so that Z_{DR} observations are expected to be free of systematic biases. The KOUN system is the most appropriate radar system for establishing this relationship because it is equivalent to each system in the operational WSR-88D network. Figure 2 shows vertical cross sections of Z_H for the five cases of deep convection used and a scatterplot of the
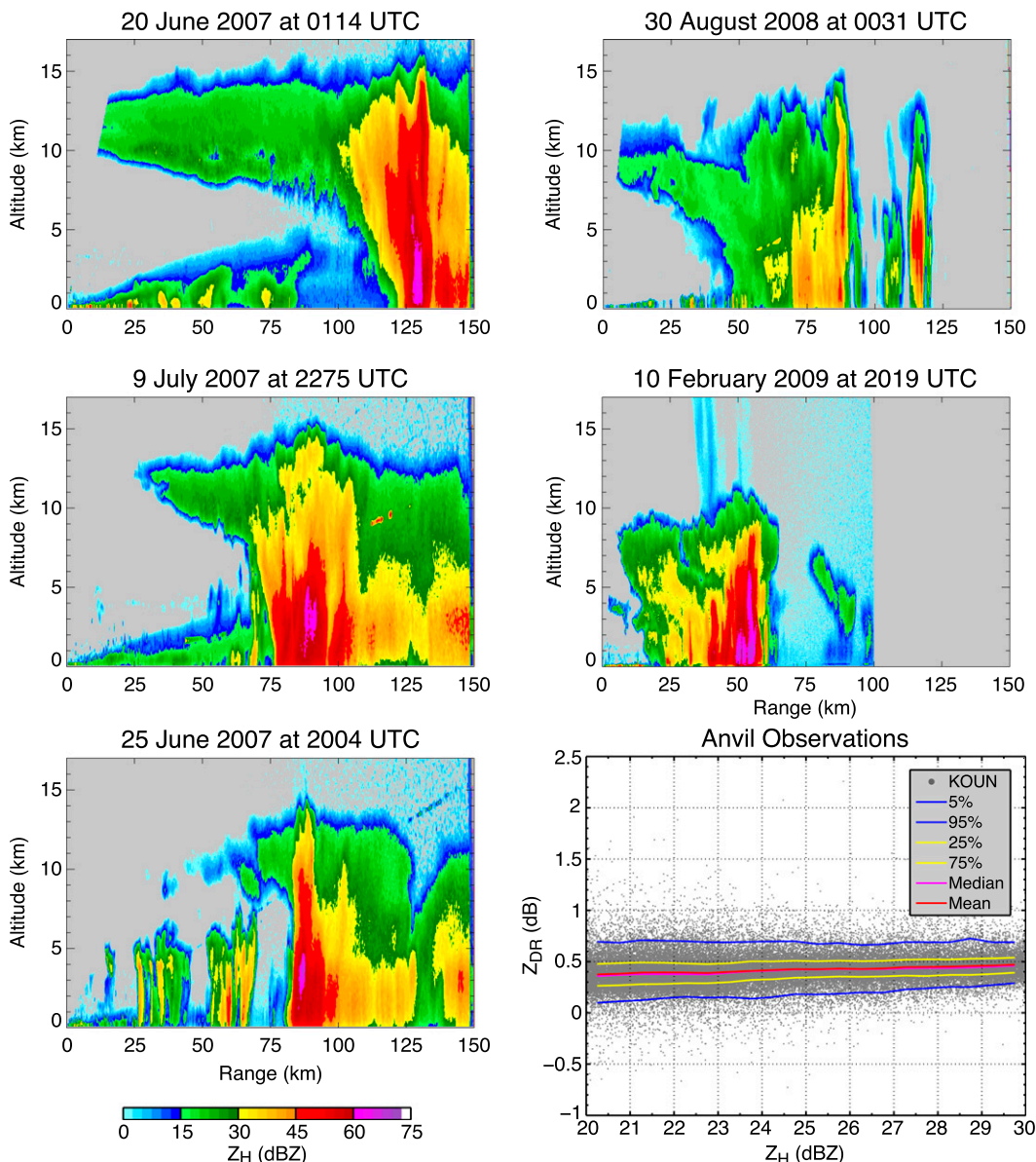
FIG. 2. Vertical cross sections of Z_H and a scatterplot comparing Z_{DR} to Z_H for observations in the anvil of deep convection from five cases observed by the NEXRAD research WSR-88D at KOUN. Blue, yellow, magenta, and red lines show the 5th and 95th percentiles, 25th and 75th percentiles, 50th percentile (median), and mean Z_{DR}, respectively, as a function of Z_H for 0.5-dBZ bins centered on each bin range.

more than 175 000 coincident Z_{DR} and Z_H anvil observations. These observations illustrate that the scattering properties of snow aggregates in the anvil region of deep convection vary little over the 20–30-dBZ range, with mean values between 0.35 and 0.45 dB and a range of values largely limited to ±0.1 dB from the mean. This mean relationship is similar if each KOUN case is analyzed separately, while the range of values is sensitive to the sample size for each case. Using this relationship from KOUN, we identify and correct for Z_{DR} biases for each radar prior to compositing and on a case-by-case

basis (i.e., for each period of continuous rain observation). Table 1 lists the ranges of identified systematic Z_{DR} biases during the study period for all WSR-88D systems used.

In addition to systematic biases, there are common observational sources of error that can bias the polarimetric fields, particularly downrange of an observed convective core. Differential attenuation of the horizontally and vertically polarized beams, though possible in heavy precipitation at S band (e.g., Ryzhkov et al. 2013; Kumjian 2013c), is extremely unlikely in the upper

TABLE 1. Ranges of identified systematic Z_{DR} biases for NEXRAD WSR-88D stations used in this study.

ICAO station ID	Bias (dB)
KAMA	−0.25 to +0.05
KDDC	−0.35 to +0.15
KDMX	−0.10
KDYX	−0.35 to −0.05
KEAX	−0.25 to −0.15
KFDR	−0.35 to −0.10
KFWS	−0.45 to −0.35
KGLD	−0.65 to −0.45
KICT	−0.15 to −0.05
KINX	−0.15 to 0.00
KLBB	−0.50 to −0.40
KLNX	−0.70 to −0.60
KLZK	0.00 to +1.15
KMAF	−0.35 to −0.25
KOAX	−0.75
KSGF	−0.35 to −0.20
KSHV	−0.25 to −0.05
KSRX	−0.60 to −0.35
KTLX	−0.85 to −0.70
KTWX	−0.05 to 0.00
KUEX	−0.50 to −0.40
KVNX	−0.50 to −0.15

portions of overshooting storms since the majority of the beam propagation path is through ice hydrometeors. Specific differential attenuation in dry ice particles is also negligibly small, owing to the insignificant imaginary part of the complex relative permittivity of ice at S band. In the event that differential attenuation does occur for WSR-88D observations, it is manifested as negatively biased Z_{DR} downrange of a core of the attenuating scatterers. Nonuniform beam filling (NBF) can cause negative Z_{DR} biases for very large cross-beam gradients of measured Z_H and Z_{DR} at distant ranges, but only if the cross-beam gradients are of opposite sign (Ryzhkov 2007). These biases begin at the region of NBF and extend downrange. If both Z_H and Z_{DR} are decreasing with increasing elevation, the NBF-induced Z_{DR} bias would be positive. If there is no existing Z_{DR} gradient in the first place, there would be no NBF-induced bias in Z_{DR}. Furthermore, the range-weighting method used in the three-dimensional compositing technique in this study (outlined in section 2c) should mitigate any NBF effects present in the observations.

Previous studies have identified large Z_{DR} biases along very strong Z_H gradients caused by a mismatch between the copolar antenna patterns at H and V polarizations (e.g., Herzegh and Carbone 1984; Pointin et al. 1988). To quantitatively assess the potential for this type of error, the antenna radiation patterns for each radar used in this study must be known. Unfortunately, such measurements do not exist. However, similar

measurements were made with the prototype polarimetric WSR-88D in Norman (KOUN) by Doviak et al. (1998). They discuss how poor antenna quality (highly mismatched sidelobe levels) in the Herzegh and Carbone (1984) study likely led to the observed biases, whereas the WSR-88D antenna pattern's sidelobe levels are at least 20 dB lower. In addition, they found good matching between the H- and V-polarization radiation patterns for KOUN in the main lobe down to about −20 dB. These factors tend to mitigate potential mismatching errors for WSR-88D antennas. Heuristically, large (or even noticeable) Z_{DR} biases owing to antenna pattern mismatching are not widely reported or observed. Given these findings, plus the fact that numerous radar systems, viewing angles, and storm structures are averaged in creating the composites shown herein, we believe that antenna radiation pattern mismatching is likely a negligible source of error in our analysis.

Random fluctuations of the polarimetric variables are expected to average out to zero over the large number of cases analyzed in this study. For example, reduced ρ_{HV} and/or low signal-to-noise ratio (SNR) will increase the standard deviation of the Z_{DR} estimates (e.g., Doviak and Zrnić 1993; Bringi and Chandrasekar 2001); however, there is no preferential bias to positive or negative values for increased standard deviation, so the noisy fluctuations will average out to zero. Last, depolarization can cause radially oriented streaks of positive or negative Z_{DR} when ice crystals are oriented at a nonzero angle relative to the polarization plane axes (e.g., Ryzhkov and Zrnić 2007). These depolarization streaks are most evident downrange of the depolarizing medium, often observed in anvil echoes downrange of a convective core. However, the large number of storms used in the composite in this study would tend to cause the Z_{DR} biases owing to depolarization to average out to zero. In other words, it is very unlikely that with different radar viewing angles and storms, the geometry of oriented crystals would be such that the depolarization-induced Z_{DR} bias was persistently negative or positive. Based on these known characteristics of observational error, we are confident that neglecting these error sources is reasonable for the analysis in this study, because (i) random errors will be averaged out over the large number of cases used, (ii) the different radars and radar viewing angles should lead to no preferred bias for the geometry-dependent artifacts, and (iii) many of the biases are often most pronounced downrange of a convective core containing mixed-phase precipitation.

c. Compositing methods

For analysis, we merge data from individual radars into high-resolution three-dimensional composites following

the methods outlined in Homeyer (2014) with some modifications. Homeyer (2014) combines radar measurements from several radars by sorting all contributing observations in a given grid column by their native central beam altitudes, followed by linear interpolation of sorted fields to a uniform vertical dimension for analysis. This approach takes advantage of the increased vertical sampling from the combination of several radars to provide a representation of the vertical extent of deep convection with altitude uncertainties less than about 500 m. These composites use observations out to 300 km in range from each radar, which allows for analysis of precipitating systems at $Z_H \gtrsim 10\,\mathrm{dB}Z$ (the minimum detectable Z_H for a WSR-88D system at 300 km is approximately 7.5 dBZ). Although the methods in Homeyer (2014) are successful in providing an accurate depiction of the altitude of deep convection, equal weighting of contributing beams in altitude can introduce nonphysical variations in the polarimetric radar variables within a given storm. Because the goal of this study is to identify the microphysical characteristics within overshooting convection, improvements to the method in Homeyer (2014) are required.

In this study, we follow the method of preserving the native altitudes of radar scans first introduced by Homeyer (2014) while weighting contributing observations in the vertical dimension by distance (range) from the radar locations. The approach of distance weighting has been explored in previous studies that produce three-dimensional composites of radar data and is used primarily to retain spatial scales that are adequately sampled from one radar while preventing retention of corresponding observations from additional radars that are undersampled (e.g., Trapp and Doswell 2000; Zhang et al. 2005; Langston et al. 2007). Following the extensive evaluation of various distance-weighting methods by Trapp and Doswell (2000), we employ the Barnes (Gaussian) weighting scheme, given as

$$w(r) = \exp\left(-\frac{r^2}{150^2}\right), \tag{1}$$

where the weight w is only a function of range from a radar location r (km), and 150 km is the e-folding range (i.e., where $w = 1/e$). Figure 3 shows this weighting function out to 300 km in range from a radar. A sensitivity test (not shown) reveals that changes in the internal characteristics of a storm from varying the e-folding range are minimal for ranges less than 150 km, while ranges significantly greater than 150 km show much less detail (i.e., more smoothing). In addition, retention of information on the vertical and horizontal extents of a storm from all radar observations requires that weights at the farthest ranges from a radar (300 km in this study) be
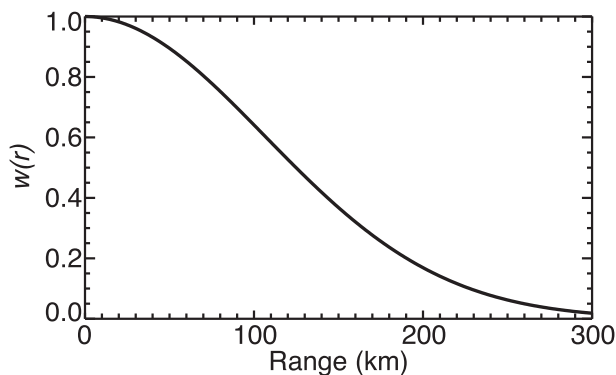

FIG. 3. The distance-weighting function used for three-dimensional compositing of radar data in this study.

significantly greater than zero (i.e., the e-folding range must be greater than about 110 km). Following the choice of e-folding range, minimizing the uncertainty and bias of the vertical extent of convection in the radar composite involves analysis of the cumulative observational weight required for retention of a binned observation, which is outlined in further detail below.

The composites in this study are made using a longitude–latitude resolution of 0.02° (~2 km) and a vertical resolution of 1 km, with contributing beams binned into each vertical 1-km grid cell that the depth of a beam overlaps. Because the vertical depth of a beam increases with increasing range, more weight is given to beams that cover fewer grid boxes and resolve shallower features within a storm. In addition, the maximum depth of influence allowed for any measurement is 1.5 km (± 0.75 km from beam center) in order to further preserve the highest resolved features from contributing observations at shorter ranges from a radar. The value of a given radar variable from this merging of contributing radar beams in a vertical bin can be expressed as

$$v(x,y,z) = \frac{\displaystyle\sum_{i=0}^{\mathrm{nrad}} w(r_i) v_i(x,y,z)}{\displaystyle\sum_{i=0}^{\mathrm{nrad}} w(r_i)}, \tag{2}$$

where nrad is the number of radars contributing to the bin, $w(r_i)$ is the distance weight for each radar observation [from Eq. (1)], and v_i is the value of the observed variable from each radar. As illustrated below, this distance-weighting approach is especially beneficial for combination of the polarimetric variables, which can be significantly degraded at far ranges where the minimum detectable reflectivity increases and SNR becomes small. Also, beam broadening effects such as NBF become more

prevalent at distant ranges. Prescribing less weight to these distant scans with potentially degraded data quality will mitigate detrimental effects on the resulting composite.

One additional improvement of the method outlined in Homeyer (2014) is an updated approach for interpolation of the radar fields in time prior to compositing. Previously, the central time of each volume scan was used as the reference time for interpolation. However, for representation of internal storm characteristics, a method that performs time interpolation separately for each elevation of a volume scan allows for proper alignment of the radar variables in each vertical column and better preserves the maxima and minima in the radar variables (i.e., less inherent smoothing). We perform this time interpolation for each elevation of a volume scan on the native radar grid prior to compositing.

A requirement associated with the introduction of a distance-weighted binning method for three-dimensional radar compositing is the evaluation of the sensitivity and accuracy of the vertical extent of deep convection determined from Z_H to the cumulative weight in each composite bin. In the Homeyer (2014) method, grid points without a detected rain feature in each radar volume were allowed to influence the composites by being set to a default value of $-33\,dBZ$ in order to provide the best determination of storm-top height from the dense overlapping of contributing radar beams. For the vertical binning approach in this study, however, radar beams without detected rain features are not allowed to influence the grid points, since setting those points to default values can introduce significant biases in the polarimetric fields, especially near the boundaries of the detected storm. We have evaluated the sensitivity of the vertical extent of deep convection to the cumulative weight in each bin and have found that retaining bins with a cumulative weight of 0.33 or greater produces results consistent with composites employing the original method in Homeyer (2014) and with high-vertical-resolution observations from space-borne radar observations (not shown). All observations retained for analysis in this study require this minimum bin weight of 0.33, which is equivalent to that from a single measurement at about 158 km in range from a radar or a native beam depth of about 2.6 km.

To examine the fidelity of the updated compositing methods, we present a vertical cross-sectional comparison between the composite polarimetric radar fields and those observed from KOUN for a deep convective storm at 0523 UTC 27 April 2013 that is overshooting the level of neutral buoyancy but not the tropopause (as determined from model analyses; see section 3). The observed vertical cross section from KOUN is the result of
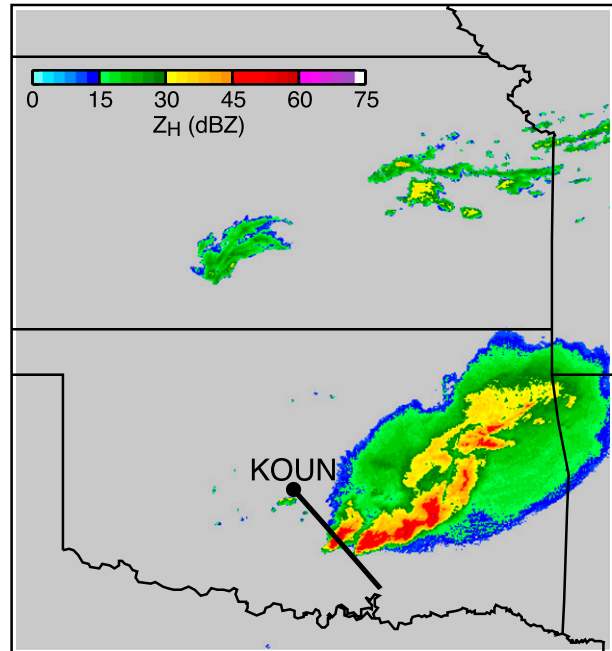

FIG. 4. Column-maximum Z_H from the WSR-88D composite valid at 0525 UTC 27 Apr 2013. The location of the NEXRAD research WSR-88D at KOUN and the path of the vertical cross sections in Fig. 5 are given by the black circle and thick black line, respectively.

a high-resolution range–height indicator (RHI) radar scan (i.e., fixed in azimuth and varying in elevation). The range resolution of the KOUN cross section is 250 m, and the vertical resolution attained from 720 staggered beam elevations is 62.5 m, while the resolved scales of the instantaneous radar composites produced in this study are typically 1–2 km in each dimension. These differences in scale are important to consider when comparing the observed structures within the storm. Figure 4 shows column-maximum Z_H over the study domain near the time of observation with the location of KOUN and the path of the vertical cross section superimposed. The observed convective storm is shown to be a nearly discrete cell that is detached from a larger leading-line trailing-stratiform mesoscale convective system (MCS) to the immediate east and north.

Figure 5 shows the vertical cross-sectional observations of Z_H, Z_{DR}, and K_{DP} from KOUN and the three-dimensional composites produced using the methods in Homeyer (2014) and the updated version outlined in this study. The direction of storm motion is from left to right in the vertical cross sections. In addition to the differences in scale between the observations outlined above, there is a slight time offset between the three-dimensional composites and the KOUN observation that provides additional potential for disagreement in characteristics of
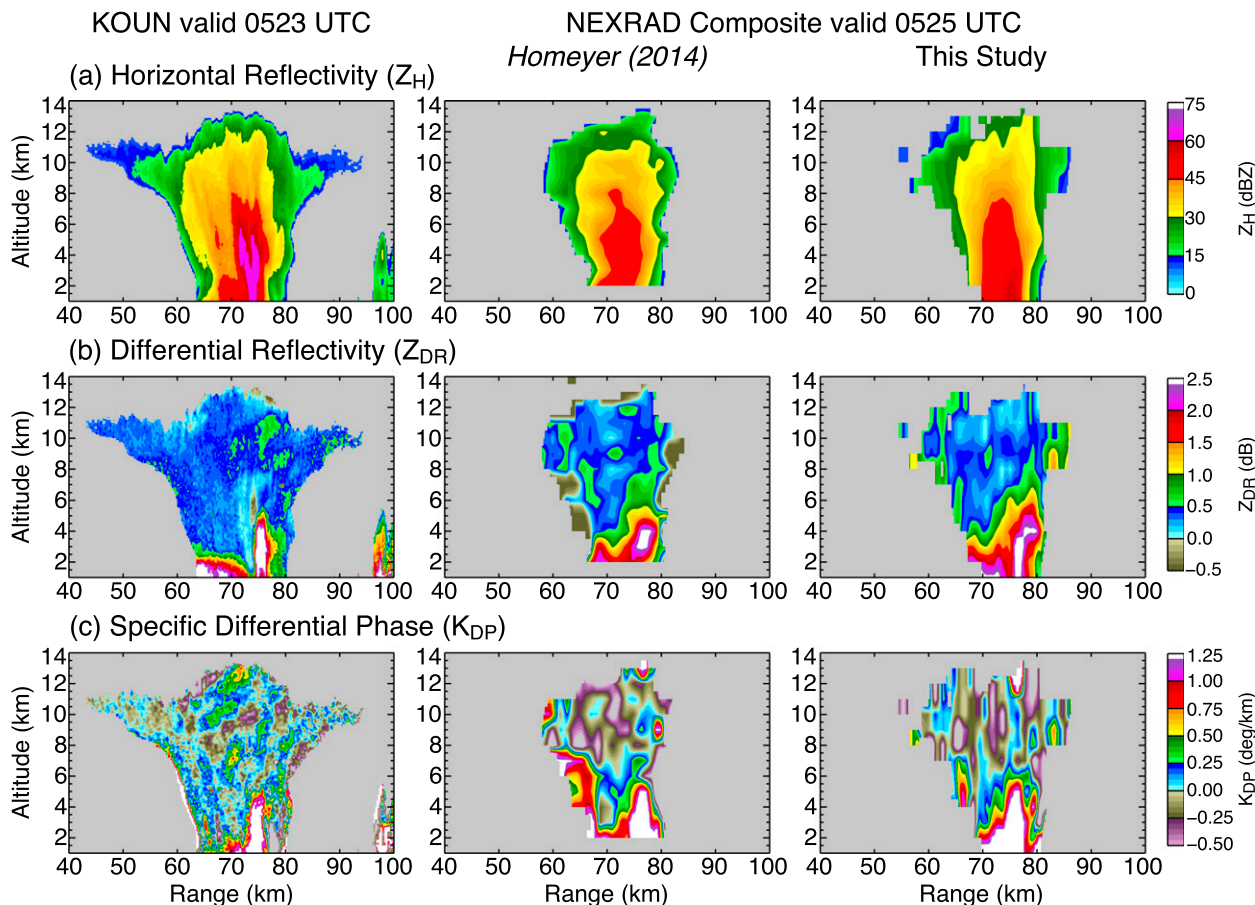
FIG. 5. A comparison of observations of (a) Z_H, (b) Z_{DR}, and (c) K_{DP} from (left) a high-resolution RHI scan completed with the NEXRAD research WSR-88D at KOUN, and a vertical cross section along the KOUN path from three-dimensional composites of operational NEXRAD WSR-88Ds using (middle) the Homeyer (2014) method and (right) the updated method outlined in this study. The observations from KOUN were taken at 0523 UTC 27 Apr 2013, and the composites represent observations at 0525 UTC.

important microphysical structures within the storm. The lack of available data from the operational radars at the exact time of the KOUN scan precludes comparison of the observations at equivalent times. Despite this slight offset in timing of the radar observations, the composite fields from the updated compositing methods used in this study show qualitatively similar features to those from KOUN. In particular, comparable magnitudes of Z_{DR} are observed at altitudes above 6 km and within the portions of the storm dominated by rain (i.e., altitudes less than 3 km and $Z_{DR} > 1$ dB). Differences between the composite and KOUN fields are greatest in the updraft region (highly positive Z_{DR} and K_{DP} columns near 75 km in range), where impacts from differences in scale and timing between the observations are apparent. The vertical depth of these column features, however, is reproduced well in the updated compositing method but is not entirely captured in the original method of Homeyer (2014). In addition, some of the unphysical maxima and minima from equal

weighting of the radar variables in altitude and assignment of default values for radar beams with no detected rain features in the original Homeyer (2014) method can be seen clearly at altitudes greater than 5 km and along the boundaries of the observed convective storm. However, despite the inadequacies of the Homeyer (2014) method for producing consistent representations of the internal storm characteristics, the vertical extent of the observed convective system is nearly equivalent between compositing methods, which are consistent with the higher-resolution KOUN observations.

3. Storm identification and classification

Following improvements of the Homeyer (2014) compositing methods, we make three-dimensional composites of the radar data at a time resolution of 1 h for analysis. The radar composites are then objectively searched for overshooting convective tops by identifying

altitude maxima of the 10-dBZ level of Z_H relative to the lapse-rate tropopause altitude. The lapse-rate tropopause altitude used is from 3-hourly operational analyses produced by the National Centers for Environmental Prediction (NCEP) for the Global Forecast System (GFS) spectral model on a 0.5° longitude–latitude grid. Tropopause altitudes provided in the GFS analysis are computed by NCEP on the native 64-level hybrid sigma-pressure vertical coordinate, which has about 500-m resolution in the tropopause region. The uncertainty in the altitude of the tropopause from the NCEP GFS analysis, as diagnosed from comparisons with high-resolution radiosonde observations, is proportional to the vertical resolution of the model (e.g., Homeyer et al. 2010). In addition, although elevation of the tropopause from diabatic processes in deep convection is often captured in the NCEP GFS analysis, the overshooting depth identified using these tropopause altitudes may be slightly exaggerated in some cases. Previous studies suggest that increases in the altitude of the tropopause near deep convection are often limited to about 1 km (e.g., Homeyer et al. 2014a).

For composite-mean analysis of overshooting convection, responsible storms are manually separated into three distinct classes outlined below:

- Organized convection includes any convective system that contains multiple convective cells embedded within a single radar-observed rain region at 2 km in altitude. These include large MCSs, which are defined as systems with a horizontal-length scale exceeding 100 km, and smaller convective lines and complexes.
- Discrete ordinary convection includes isolated convective storms that do not contain a mesoscale rotation in the radar-observed Doppler velocity fields. These convective storms are typically small in horizontal scale, initiate in early to late afternoon, and may evolve into organized convective systems that persist overnight.
- Discrete supercell convection includes isolated convective storms that do contain mesoscale rotation and are often characterized by low-altitude hook features in Z_H. In addition, these storms typically contain some of the largest and most intense updrafts in midlatitude convection.

We retain observations of overshooting convective storms if their echo tops ($Z_H \geq 10$ dBZ) reach at least 1 km above the altitude of the lapse-rate tropopause. This requirement ensures that the combined uncertainty from the radar-derived altitude (~500 m) and NCEP GFS lapse-rate tropopause (~500 m) is less than the overshooting depth. Upon objective identification of overshooting tops, vertical cross sections of the

three-dimensional composite radar fields are taken along a path that extends from the storm updraft into the outflow/anvil region downstream, for which subjectivity is required to determine the orientation of the cross-sectional path relative to the identified overshoot. The location of the convective updraft in each case is determined primarily through identification of known signatures in the polarimetric radar variables, such as deep columns of highly positive Z_{DR} and K_{DP}. These vertical cross sections are combined for storms in each classification to produce composite-mean states, offering robust microphysical representations of an overshooting storm.

Figure 6 shows example vertical cross sections of Z_H, Z_{DR}, and K_{DP} taken through overshooting storms in each classification. The example cross sections for organized convection (Fig. 6a) and discrete ordinary convection (Fig. 6b) contain deep Z_{DR} columns extending to altitudes above 5 km that allow direct identification of the updraft location. For the organized convection case, the vertical cross sections bisect a leading-line trailing-stratiform MCS propagating from northwest to southeast over northern Kansas. In this case, convective updrafts are embedded within the leading edge of the convective line, resulting in cross sections taken east to west. The discrete ordinary convective storm is located to the south of an MCS in central Kansas and is also translating from west to east. Because the storm updraft is located in the southwestern portion of the storm, the vertical cross sections are taken west to east in this case. It is important to note here that although the column-maximum reflectivity map would suggest this discrete convective storm is embedded within the rain region of the MCS to the north, reflectivity observations at an altitude of 2 km show a clear separation between this storm and the nearby MCS that allows the classification of discrete ordinary convection in this case. Figure 6c shows an example discrete supercell convective storm, which is propagating from west to east over central Oklahoma. This particular supercell storm produced a long-lived tornado at the highest intensity rating on the enhanced Fujita scale (EF5) that devastated the town of Moore, Oklahoma, resulting in at least 2 billion U.S. dollars in property damage and 24 fatalities (http://www.ncdc.noaa.gov/stormevents/eventdetails.jsp?id=451572). Although this supercell convective storm does not contain a deep column of highly positive Z_{DR} or K_{DP} at this time, it does show an additional radar feature observed in Z_H that allows identification of the storm updraft: a bounded weak-echo region (BWER) extending up to around 3 km in altitude (identified by the black ellipse in Fig. 6c). BWERs are common signatures of supercell storms, representing a location of
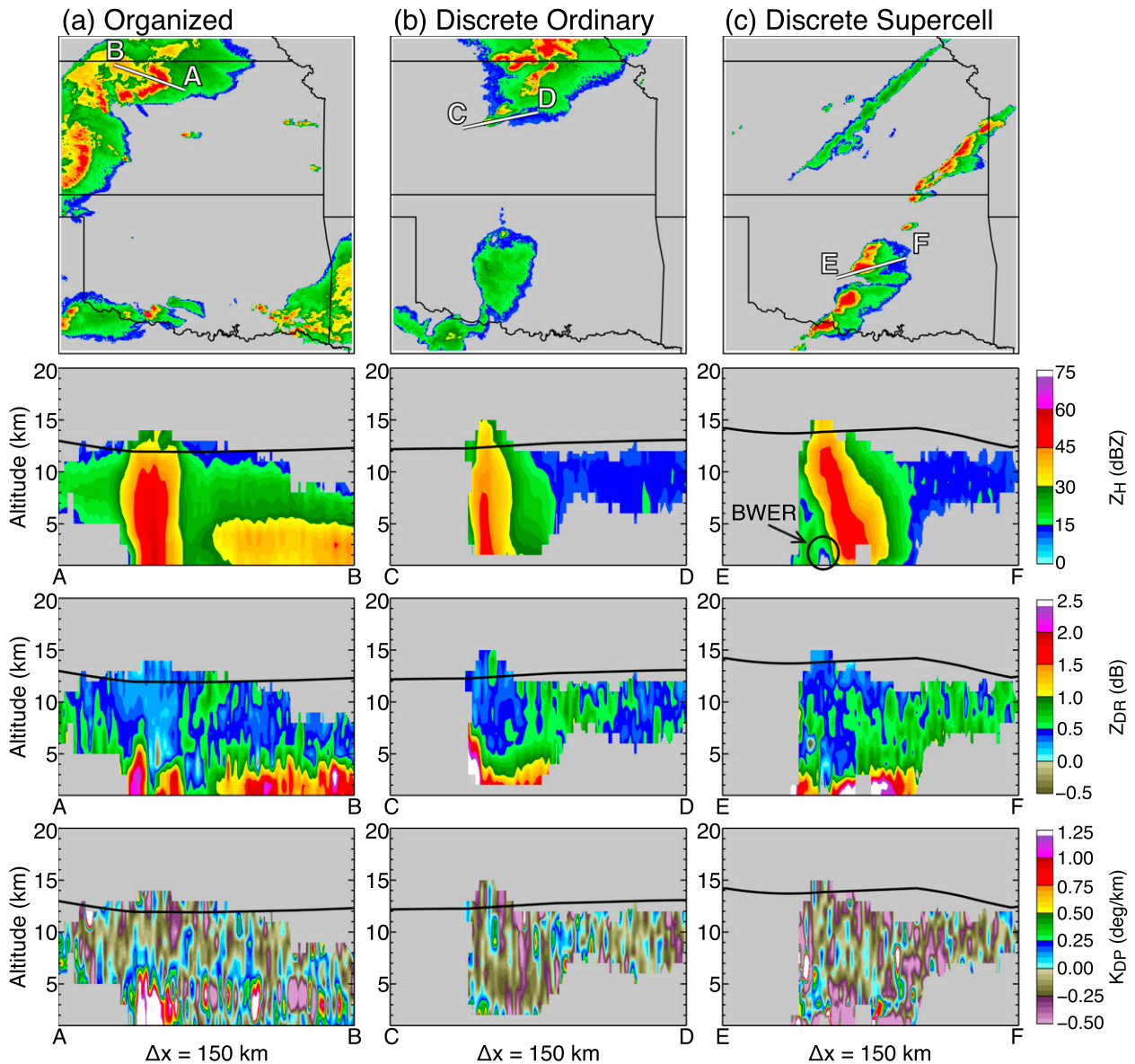
FIG. 6. (top)–(bottom) Maps of column-maximum Z_H and vertical cross sections of Z_H, Z_{DR}, and K_{DP} for examples of (a) organized convection valid at 0300 UTC 17 Jun 2013, (b) discrete ordinary convection valid at 0200 UTC 28 May 2013, and (c) discrete supercell convection valid at 2000 UTC 20 May 2013. The thick black lines in the vertical cross sections show the NCEP GFS analysis tropopause altitude. The locations of the vertical cross sections are given by the thick white lines labeled A–B in (a), C–D in (b), and E–F in (c).

strong upward motion and, consequently, limited fall-out of hydrometeors to lower altitudes [e.g., Musil et al. (1986) and references therein]. The Z_{DR} and K_{DP} columns were observed for this storm at times before and after that shown in Fig. 6c, which coincided with a collapse in the column features that is inherent to the life cycle of a deep convective storm (e.g., Kumjian et al. 2014). In addition, there is an example in Fig. 6c of an observation with bin weight less than 0.33 below 4 km and near the center of the horizontal axis that was excluded from analysis.

4. Results

a. Characteristics of overshooting

Analysis of the polarimetric radar composites during March–June 2013 reveals more than 400 overshooting storms within the study domain. The locations of identified overshooting convective tops for each storm classification are shown in Fig. 7. Overshooting storms are common throughout the domain, with apparent clustering of storms to the west and north during the analyzed time period. There is also distinct seasonality
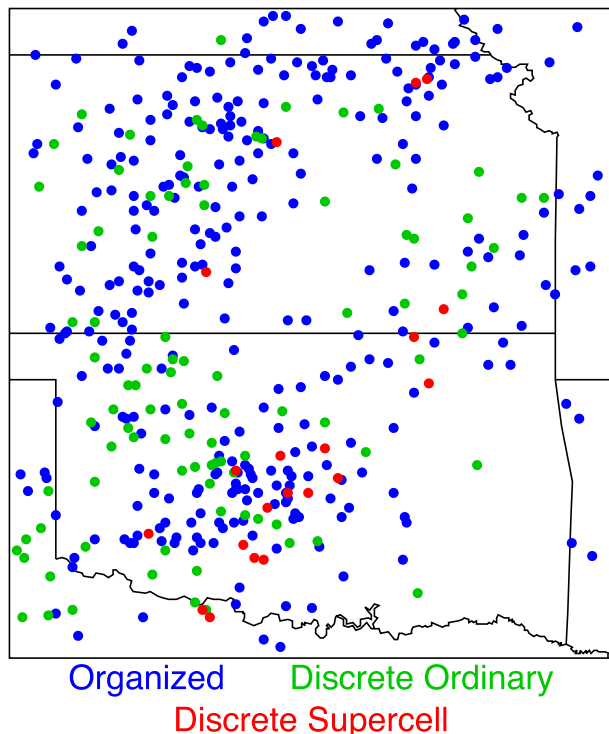
FIG. 7. A map of the locations of overshooting storms analyzed in this study, colored by storm classification. Organized (blue), discrete ordinary (green), and discrete supercell (red) convection are shown.

observed, with more than half of the identified cases occurring in May, the most active month for convection in the study domain. Table 2 lists the number of identified storms by month and classification. Because the map and seasonality represent storms identified during one spring/early summer season, it is unlikely that this distribution is representative of a long-term climatology. Organized convection accounts for about three-quarters of identified overshooting storms, followed by discrete ordinary convection and supercell convection. A characteristic that is in agreement with known characteristics of deep convection is the observed diurnal cycle, given in Table 3. In particular, there is a distinct frequency maximum near 1800 central daylight time (CDT), coincident with the typical time of maximum surface temperature and largest instability or convective available potential energy (CAPE). In comparison, the overshooting frequency minimum is found in early to late morning and corresponds to the typical time of minimum surface temperature and convective inhibition.

In addition to their geographical distribution and seasonal and/or diurnal cycles, the physical properties of overshooting convection for each storm classification provide details on their characteristic size and transport

TABLE 2. Number of identified overshooting storms by month and classification.

| Month | Classification | | | |
	Organized	Discrete ordinary	Discrete supercell	Total
March	6	1	0	7
April	71	16	0	87
May	161	69	19	249
June	78	8	1	87
Total	316	94	20	430

potential. Figures 8a and 8b examine two of these physical characteristics for each storm classification: overshooting depth and the diameter of the overshoot, respectively. In Fig. 8a, the most frequent depth for organized convection is 2 km, with the majority of storms ranging from 1 to 5 km above the tropopause. Discrete ordinary convective storms show similar ranges of overshooting depth, with a frequency maximum 1 km higher than that for organized convection. Discrete supercell convection shows the broadest distribution, with depths ranging from 1 to 8 km and a frequency maximum of 2–3 km. Although these distributions illustrate a higher likelihood of overshooting deeper than 3 km for supercells, which is expected based on their association with stronger updrafts, the number of supercell storms identified for analysis is significantly lower than that for the other classifications (20 storms). Note also that the few cases of exceptionally deep overshooting (>6 km) do not coincide with environments where the tropopause is very low. Rather, such cases represent storms that reach altitudes of 18–19 km.

Figure 8b shows scatterplots of the equivolume diameter of overshooting tops as a function of their identified overshooting depth. The equivolume overshoot diameter is that assuming the observed radar volume (at altitudes greater than 1 km above the tropopause) is distributed evenly over the identified overshooting depth. The observed distributions for each

TABLE 3. Number of identified overshooting storms by time and classification.

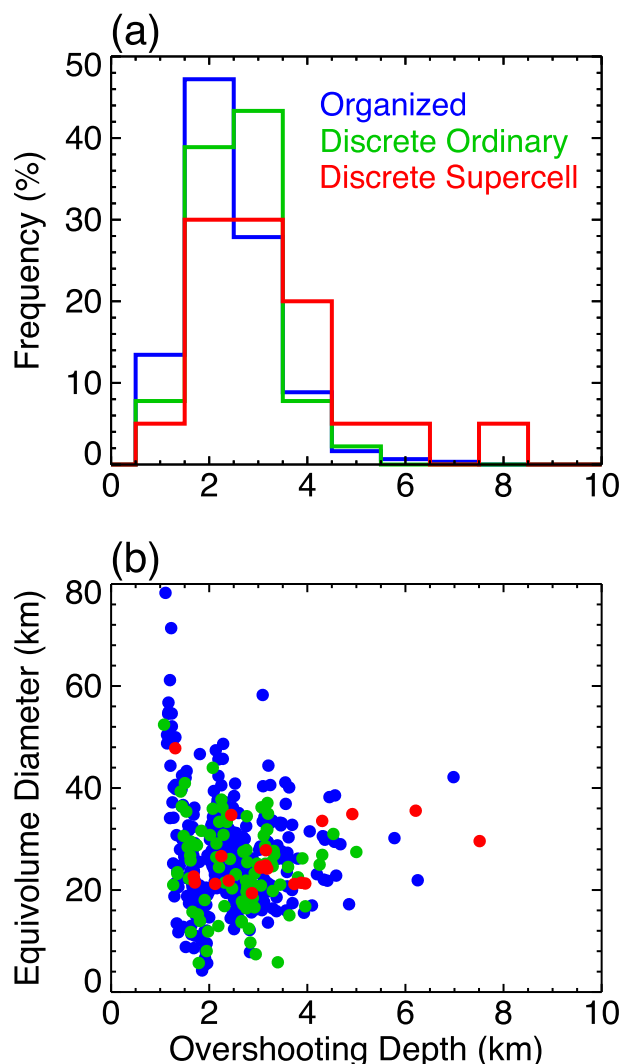| Time (CDT) | Classification | | | |
	Organized	Discrete ordinary	Discrete supercell	Total
0000–0200	30	1	0	31
0300–0500	21	2	0	23
0600–0800	15	0	0	15
0900–1100	9	1	0	10
1200–1400	8	5	0	13
1500–1700	48	30	14	92
1800–2000	119	46	5	170
2100–2300	66	9	1	76

FIG. 8. Distributions of (a) storm frequency and (b) equivolume diameter of the overshooting top as a function of overshooting depth and colored by storm classification. Organized (blue), discrete ordinary (green), and discrete supercell (red) convection are shown.

storm classification show similar relationships, with an apparent increase in the diameter of overshooting tops as the depth of overshooting increases for depths greater than about 2 km. In addition, there is a significant increase in the spread of overshoot diameter with decreasing overshooting depth for each classification that is likely the result of tropopause error, which (if biased low) may allow portions of the anvil region adjacent to the overshooting top to be included in this diagnostic. Apart from the large spread in overshoot diameter near the 1-km overshooting-depth threshold, the overshooting tops identified in this study span diameters from about 5 to 40 km. Also, despite potentially stronger updrafts in discrete supercell convective storms, these

distributions do not suggest that the overshooting convective core is larger than that at similar depths in the remaining classifications.

b. Microphysical characteristics of storm classifications

Figures 9a–c show composite-mean vertical cross sections of Z_H, Z_{DR}, and K_{DP} in relative distance to the location of the overshooting top from radar observations and in relative altitude to the NCEP GFS lapse-rate tropopause for each storm classification. To limit spurious features from small sample sizes, only bins with observations from at least one-third of the total number of identified storms in each case are shown. It should be emphasized here that these composite means are not representative of the physical characteristics of an individual storm and, as a result, may differ considerably from the behavior expected of a single case. Rather, the composites represent the most common characteristics observed throughout the convective core and adjacent anvil regions of the storms analyzed in this study. Moreover, this analysis is focused on one specific type of convection: that which overshoots the altitude of the tropopause. For justifiable reasons outlined in reference to observed characteristics in the analysis below, these composites may not be generally representative of deep convection.

There are distinct features consistent across all storm classifications observed in the composite-mean polarimetric fields. Notably, the previously outlined columns of highly positive Z_{DR} and K_{DP} coincident with the storm updraft location are clearly shown, located in the −15- to +15-km overshoot-relative distance range and extending up to around 6 km below the tropopause. With consideration of differences in the mean tropopause altitude for storms in each classification (12.5 km for organized and discrete ordinary convection, 13.5 km for discrete supercell convection), these column features are deepest and widest for discrete supercell convection, at altitudes up to 2 km higher than the remaining classifications and in agreement with typically stronger and larger convective updrafts in supercell storms. Larger Z_{DR} values are found at higher altitudes in the supercell classification as well, indicating more supercooled liquid water present on or in ice particles and/or larger raindrops being lofted higher by the more intense updrafts. The K_{DP} column values are not as large in the supercell case, possibly owing to the spatial offset between K_{DP} and Z_{DR} columns typical of supercell storms (e.g., Kumjian and Ryzhkov 2008) or contamination from random noise, since the sample size is relatively small.

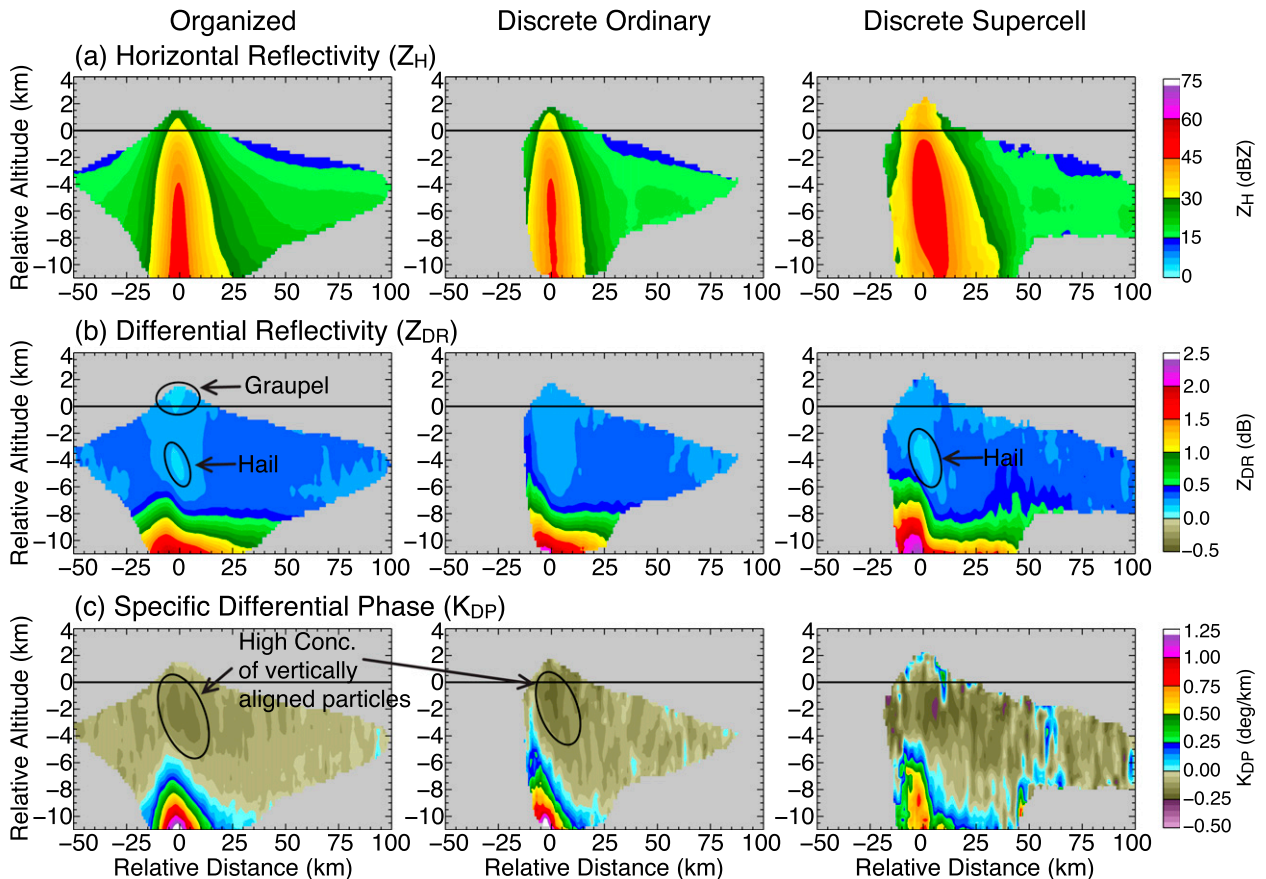Another common polarimetric feature among storm classifications is the near-zero (0.1–0.3 dB)-Z_{DR} region

FIG. 9. Composite-mean vertical cross sections in distance relative to the maximum altitude of the overshooting top and in altitude relative to the NCEP GFS lapse-rate tropopause of (a) Z_H, (b) Z_{DR}, and (c) K_{DP} for (left) organized, (middle) discrete ordinary, and (right) discrete supercell convection. Means are calculated using all observations within 2 km of the vertical cross-sectional path. Only bins with contributing observations from at least one-third of the total number of identified storms for each classification are shown.

throughout the upper portions of the convective core, covering overshoot-relative distances from -10 to $+10$ km and tropopause-relative altitudes from -7 to $+2$ km. These low-Z_{DR} regions suggest the presence of nearly isotropic hydrometeors (e.g., graupel or hail). There are two distinct minima within the near-zero-Z_{DR} regions that highlight unique storm microphysical signatures. In particular, one feature that is commonly observed in deep convection is the Z_{DR} minimum located immediately downstream and above the Z_{DR} and K_{DP} column features, centered near 0-km overshoot-relative distance and near 4 km in altitude below the tropopause. This near-zero-Z_{DR} feature, which is often negative in individual storms, is likely indicative of large, wet hail within the convective updraft (e.g., Balakrishnan and Zrnić 1990). The Z_{DR} minima at these altitudes are most distinct in the composite means for organized and supercell convection classifications (identified by black ellipses in Fig. 9), and are confined to $Z_H \geq 40$ dBZ, further verifying their association with

large hail. The second minimum in Z_{DR} is observed throughout the overshooting top in the organized convection case. This near-zero-Z_{DR} feature is characteristically different than that corresponding to hail at altitudes below the tropopause and is found primarily in regions of Z_H ranging from 15 to 30 dBZ. For the observed Z_H range in this case, hydrometeors responsible for the low Z_{DR} could be small hail, lump and/or conical graupel, or snow aggregates (e.g., Aydin and Seliga 1984; Vivekanandan et al. 1999). However, hail and graupel are the most likely candidates in this case, since formation of aggregates is only possible when the vertical velocity is sufficiently weak, allowing the largest crystals to fall and gradually collect smaller crystals. Thus, aggregates are almost entirely limited to detraining anvil regions in deep convection.

Despite often suffering from random noise in instantaneous observations, the composite-mean K_{DP} fields for the organized and discrete ordinary convection classifications show coherent and strongly negative
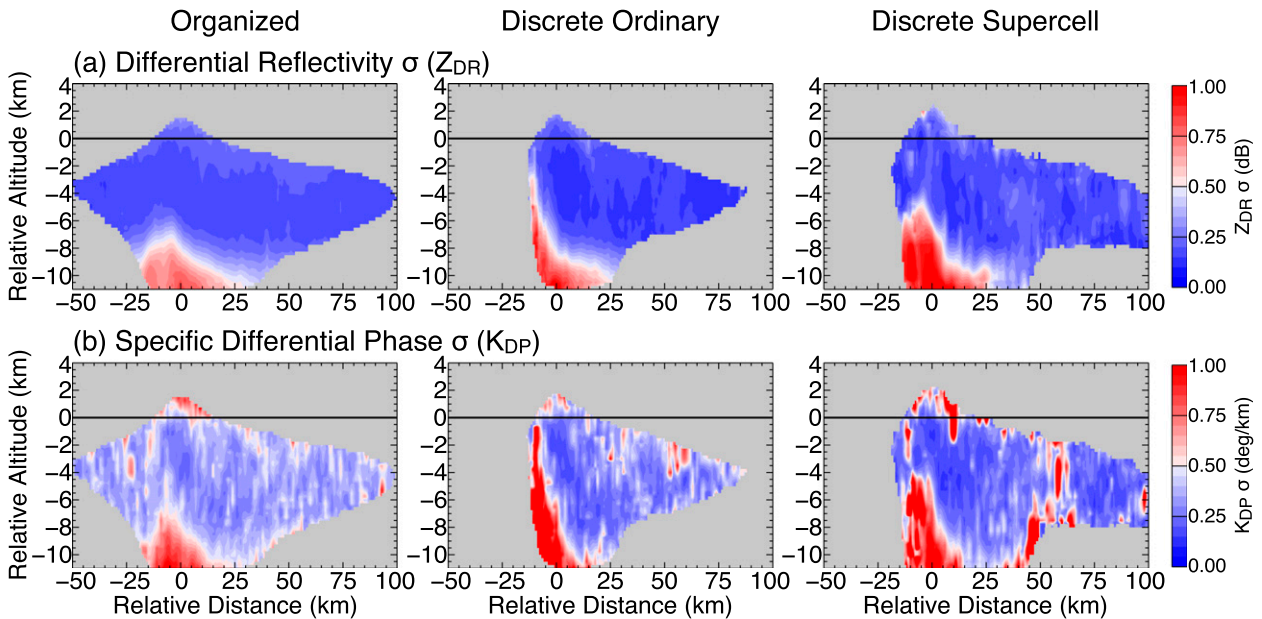
FIG. 10. Standard deviations σ from the composite-mean vertical cross sections in Fig. 9 of (a) Z_{DR} and (b) K_{DP}.

features ($-0.1°$ to $-0.2°\,km^{-1}$) at slightly higher altitudes than the minimum-Z_{DR} hail signatures, with broad minima located at altitudes below and within about 4 km of the tropopause. Such K_{DP} distributions suggest that a significant concentration of hydrometeors with their major axis aligned vertically (on average) coincides with the convective core, which may contribute to the reduced Z_{DR} there. It is also important to note that K_{DP} observations are slightly negative throughout the anvil regions in the composites, which is not typical for an instantaneous observation of deep convection. Negative K_{DP} is common in a convective storm where there is vertical alignment of ice crystals along an electric field. Such alignments are often limited in scale and lifetime, with increasingly negative K_{DP} over time and up to the point of discharge (i.e., a lightning flash). The result of this time evolution of K_{DP} is to increase the likelihood of a negative observation in an electrically active storm, since positive K_{DP} values following a discharge persist for a short time as the electric fields reestablish (e.g., Caylor and Chandrasekar 1996). Despite the irregularity of pervasive negative K_{DP} (or vertically aligned ice) in the upper regions of deep convection, there have been a number of documented cases in the past (e.g., Zrnić et al. 1993; Caylor and Chandrasekar 1996; Tessendorf et al. 2007; Lang and Rutledge 2008; Dolan and Rutledge 2010; Ventura et al. 2013). In this study, we are analyzing a unique type of storm that is often characterized by large updraft volume and velocity and large graupel concentrations, which are two established characteristics of the most electrically active convective

storms (e.g., Tessendorf et al. 2007; Deierling and Petersen 2008; Calhoun et al. 2013). Thus, it is likely that the negative K_{DP} throughout the anvil region observed in the composites is real and associated with the high frequency of lightning in such storms. In addition, the K_{DP} minima coincident with low Z_{DR} in the upper levels of the convective core may (in part) suggest significant concentrations of conical graupel in these storms.

To further examine the appropriateness of identified microphysical features in the composite-mean cross sections of Fig. 9 and to evaluate the impact of neglected observational sources of error on the polarimetric fields outlined in section 2b, standard deviations from the composite-mean Z_{DR} and K_{DP} for each storm classification are shown in Figs. 10a and 10b, respectively. These cross sections imply that observational sources of error do not routinely contaminate the composite-mean storm analysis in this study. In particular, the spread of values for bins in the upper altitudes of each composite storm is small (<0.2 dB for Z_{DR}) and shows little variation with overshoot-relative distance. If observational sources of error in Z_{DR} were common, known relationships of the induced biases relative to the convective core would imply that the spread in the polarimetric fields should be largest in the outward anvil regions, which is not observed here. The largest spread in the polarimetric variables is observed in the updraft region for each case, where the magnitudes of Z_{DR} and K_{DP} are typically largest and the depth and width of related column features are known to vary significantly with storm scale and life cycle (e.g., Kumjian et al. 2014).

Alternatively, the smallest deviations for both polarimetric variables are observed throughout the storm anvil and within the near-zero-Z_{DR} and negative-K_{DP} region of the convective core. These deviations provide confidence in the identified microphysical characteristics outlined above, especially at these below tropopause altitudes.

One important feature in the cross sections from Fig. 10 is that the spread in each polarimetric variable generally increases with increasing altitude in the overshooting top. Comparison with the characteristics observed in the composite-mean cross sections in Fig. 9 allows for evaluation of observational sources of error for this increase in Z_{DR} and K_{DP} spread. The primary candidate for observational bias in this case is NBF, since detection of small-scale features such as an overshooting top may often occur via a partially filled radar beam. As outlined in section 2b, if both Z_H and Z_{DR} are decreasing with increasing altitude, the NBF-induced Z_{DR} bias will be positive, and if no Z_{DR} gradient exists within the overshooting top, there will be no NBF-induced bias in Z_{DR}. These known relationships dismiss the likelihood of NBF biases in this analysis, since Z_{DR} values in the overshooting top are less than those in the outward anvil regions and generally decrease in altitude for each case, which would allow for a positive NBF-induced Z_{DR} bias. As outlined above, alternative sources of observational error are typically limited to regions downrange of the convective core, and these composites do not show variability consistent with such biases.

An alternative explanation for the increased spread in Z_{DR} and K_{DP} within the overshooting top is that the microphysical distributions occupying this region may vary considerably with storm intensity and evolution. For example, Z_{DR} values within the overshooting top are lowest in the composite means for organized convection, where the overshooting depth is shallower and presumably weaker than that for discrete ordinary and supercell classifications. In addition, the inference of conical graupel and other hydrometeors contributing to the Z_{DR} signal in the organized convection case, as outlined in detail in the following section, confirms a relationship between storm evolution and the microphysical characteristics of the overshooting top.

c. Microphysical characteristics of storm evolution

Hydrometeors in a given storm cover a wide range of sizes whose growth and sedimentation affect the evolution of the storm. Further, when processes such as differential sedimentation (size sorting) alter the composition of a storm, the polarimetric variables can be significantly affected (e.g., Kumjian and Ryzhkov 2012). Based on the vertical distribution of near-zero-Z_{DR}

features identified in the storm composites in Fig. 9, it is likely that the hail signature at midlevels and graupel signature in the overshooting top correspond to different evolutionary stages of an overshooting storm, as there are distinct differences in hydrometeor size (Z_H) and implied terminal velocities between these two regions. To examine this potential relationship, we separate storms by evolution into two stages: mature and decaying. We define overshooting convective storms of any classification as mature if the maximum altitude of $Z_H \geq 40\,dBZ$ is found at or above the tropopause level and decaying if the maximum altitude of $Z_H \geq 40\,dBZ$ is limited to altitudes more than 3 km below the tropopause. These criteria aim to isolate mature storms as those that have reached their maximum vertical velocity, thus lofting the largest hydrometeors to their maximum altitude. Similarly, the criteria for decaying storms aims to isolate times where the vertical velocity has decreased following a previous maximum so that the storm is still deep (and overshooting) but the largest hydrometeors are displaced significantly in altitude below the storm top. There are 126 and 210 storms contributing to the composites for mature and decaying overshooting convection, respectively. In addition, since composites are only made at 1-h intervals, we cannot separately identify overshooting storms in the developing stage.

Figures 11a and 11b show composite-mean vertical cross sections of Z_H, Z_{DR}, and K_{DP} for overshooting convection in mature and decaying stages, respectively, and support the hypothesis of hydrometeor sorting outlined above, showing clear horizontal and vertical expansion of low Z_{DR} within the overshooting-top and upper-troposphere portion of the convective core in the decaying stage. In addition, the Z_{DR} composites for each stage reveal a characteristic transition in the vertical structure of the low-Z_{DR} convective core. In particular, a minimum in Z_{DR} coincident with $Z_H > 45\,dBZ$ and consistent with the presence of large hail is most distinct in the mature overshooting stage, while that consistent with more isotropic lower Z_H ($<30\,dBZ$) graupel particles in the overshooting top is most distinct in the decaying stage. The highly positive Z_{DR} and K_{DP} columns indicative of the updraft location and intensity are also greatly diminished in the decaying stage, supporting the choice of mature and decaying convection classifications used in this case.

Following those presented in Fig. 10, Fig. 12 shows standard deviations from the mean Z_{DR} and K_{DP} composites in the mature and decaying overshooting convection stages presented in Fig. 11. Similar to those outlined for the composites of storm classifications, these standard deviations suggest that observational sources of error do not contaminate the composite
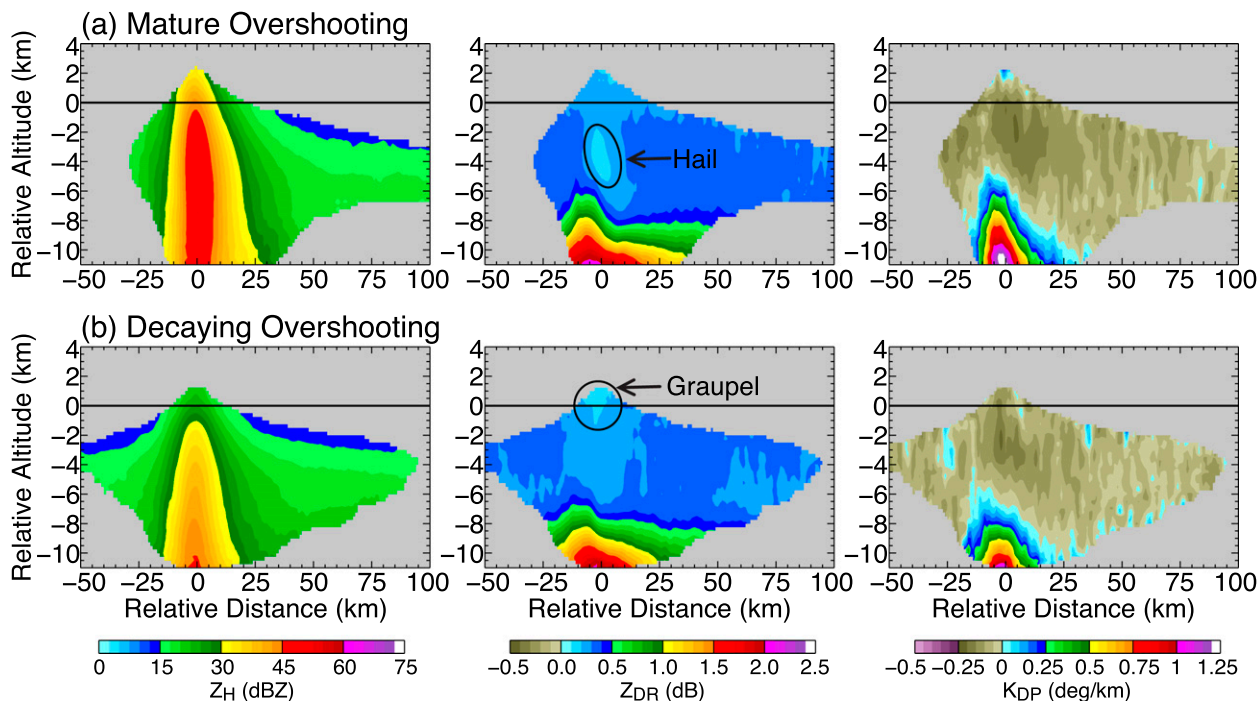
FIG. 11. Composite-mean vertical cross sections of Z_H, Z_{DR}, and K_{DP}, as in Fig. 9, for (a) mature overshooting convection ($Z_H \geq 40\,\text{dB}Z$ at altitudes above the tropopause) and (b) decaying overshooting convection ($Z_H \geq 40\,\text{dB}Z$ at altitudes more than 3 km below the tropopause).

analysis of mature and decaying overshooting convection. The largest standard deviations in the polarimetric fields remain confined to the region of the updraft and corresponding Z_{DR} and K_{DP} column features. However, in contrast to that observed for composites of storm classifications, comparisons between the mature and decaying stages reveal a characteristic change in the structure of variability within the overshooting top. Notably, the standard deviations in the overshooting top during the decaying stage are lower than those during the mature stage, providing increased confidence in the composite-mean values there. In the mature stage, standard deviations in the polarimetric fields increase with increasing altitude within the overshooting top, in agreement with the general characteristics observed for composites by storm classification in Fig. 10.

5. Summary and discussion

Novel methods for combination of the polarimetric radar variables from multiple radars into high-resolution three-dimensional composites were used to examine the microphysical characteristics of overshooting convection within a region encompassing Oklahoma and Kansas in the continental United States during March–June 2013. Over 400 overshooting storms were identified within the study domain, with a peak in the frequency of overshooting

during May. A large diurnal cycle in convective overshooting was also observed, reaching a maximum near 1800 CDT and consistent with the time of maximum surface temperature and instability.

For identification of the microphysical characteristics of overshooting convection, individual storms were grouped into three classifications: organized convection, discrete ordinary convection, and discrete supercell convection. Organized convection was found to be the most frequent source of overshooting, accounting for nearly three-fourths of all identified storms. Discrete ordinary and discrete supercell convection, however, were found to frequently reach altitudes about 1 km higher than that in organized convection, implying a higher likelihood of transport into the stratosphere in those cases. Despite often reaching higher altitudes in the discrete convection classifications, the relationship between overshooting depth and the diameter of the overshooting top was comparable for all classifications.

Vertical cross sections taken through the convective updraft and downstream anvil of each storm were combined to produce robust representations of the microphysical composition and vertical structure for each storm classification. Apart from apparent differences in the intensity between classifications, characteristics of the polarimetric variables throughout the composite storms are largely consistent. In particular, all cases
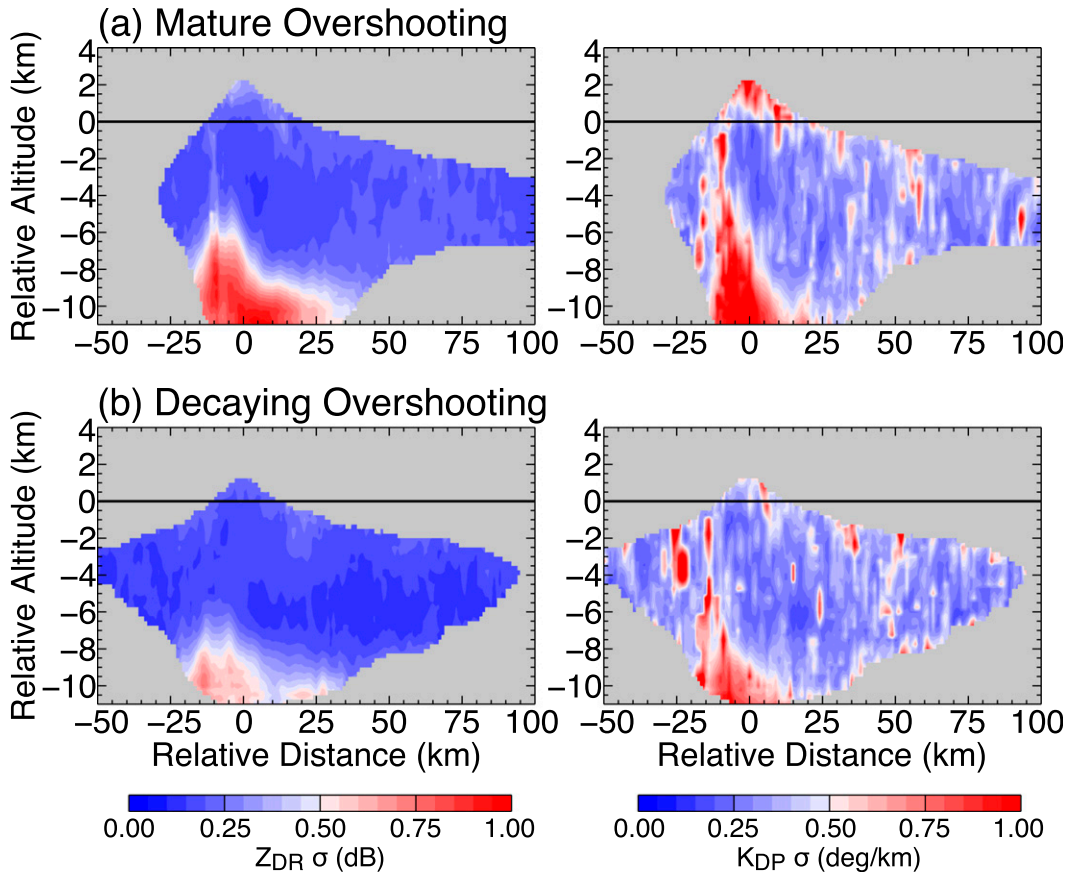
FIG. 12. Standard deviations from the composite-mean vertical cross sections of Z_{DR} and K_{DP} in Fig. 11 for (a) mature overshooting convection and (b) decaying overshooting convection.

show highly positive Z_{DR} and K_{DP} columns extending to altitudes above the melting level, consistent with lofting of supercooled liquid and rain droplets within the storm updraft. In addition, portions of the convective core at altitudes higher than the updraft features show near-zero Z_{DR} and negative K_{DP} indicative of contributions from a mixture of isotropic scatterers and hydrometeors with their major axis aligned vertically. Two distinct Z_{DR} minima within the convective core were identified as being associated with unique microphysical distributions. A minimum in Z_{DR} at altitudes slightly above and downstream of the positive column features that suggests the presence of large hail was observed for both organized and discrete supercell classifications. Individual storms sometimes exhibited negative Z_{DR} values in this region, though the composite-mean values were slightly above 0 dB. This suggests that the negative-Z_{DR} signature was present in some, but not all, of the organized convection and discrete supercell cases. A second minimum in Z_{DR} was observed within the overshooting top for organized convection and associated with Z_H values ranging from 15 to 30 dBZ,

consistent with the scattering properties of small hail and/or lump or conical graupel. In the upper-troposphere portion of organized and discrete ordinary convection, composite-mean K_{DP} distributions suggested high concentrations of vertically aligned particles within the convective core, which provided additional support for contributions from conical graupel.

To ensure that neglected observational sources of error did not impact our analysis, we examined standard deviations of the polarimetric variables from their composite-mean values in each case. The spread in the observed Z_{DR} and K_{DP} values was small relative to the identified microphysical features and did not show range-dependent fluctuations that would imply frequent contamination from observational error. Furthermore, the characteristics of the composites and spread of the observations enabled elimination of observational error as a mechanism for observed increases in the spread of polarimetric variables with increasing altitude in the overshooting top.

Analysis of the evolution of overshooting convection provided further confidence in the microphysical

distributions observed. Motivated by the relationship between fall speeds and hydrometeor size, we examined composite-mean cross sections of overshooting storms during mature and decaying stages. The unique microphysical features of hail and graupel identified in the analysis of storm classification were found to dominate the vertical structure of low-Z_{DR} and negative-K_{DP} features during the mature and decaying stages, respectively. This result is consistent with sorting of hydrometeors in a collapsing storm from differences in fall speeds and further supported the identification of conical graupel as a source for low Z_{DR} and negative K_{DP} in the uppermost levels of the convective core. Furthermore, the spread in Z_{DR} and K_{DP} values decreased considerably throughout the convective core and overshooting top during the decaying stage, providing increased confidence in the composite-mean signatures.

Although the observation of graupel within the upper portion of a convective core is not surprising (e.g., Yuter and Houze 1995; Vivekanandan et al. 1999; Rowe et al. 2011, 2012), the apparently significant concentration of conical graupel observed in this study has not been documented previously. This finding may have important implications for the cloud electrification and microphysical evolution associated with deep tropopause-penetrating convection. For example, a widely accepted theory for cloud electrification is from collisions between graupel and ice particles in the upper levels of a convective updraft (e.g., Berdeklis and List 2001; Deierling et al. 2008, and references therein). The apparent sorting of hydrometeors during the decaying stage of an overshooting top observed in this study may facilitate environments capable of efficient collisions during subsequent updraft pulses. Further, negative K_{DP} observed throughout the upper portions of all composite-mean storms in this study implies that lightning flash rates are high in these storms. In addition, because conical graupel is a common nucleus for hail growth (e.g., Knight and Knight 1973), this preconditioning of the convective column may also lead to changes in the efficiency of hail production in overshooting convection. Additional studies are required to examine the impacts of such hydrometeor sorting on these physical processes. Incorporating hydrometeor identification algorithms in future radar analyses and inclusion of lightning observations will help to shed further light on the detailed characteristics.

The finding of graupel in the overshooting top also suggests that injection of smaller hydrometeors into the lower stratosphere from the downstream anvil may be a more efficient pathway for stratospheric water vapor from overshooting convection. Because the fall speeds of frozen drops and aggregates in the downstream anvil are lower than those for graupel, they would remain in the lower stratosphere and sublimate over longer time periods than the larger hydrometeors from the overshooting top. However, the concentration of these large hydrometeors in the overshooting top is not entirely known, and they could account for a smaller fraction of hydrometeors than the radar observations would suggest. In addition, the radar observations are not capable of directly observing the cloud top, and mixing of an overshooting top into the lower stratosphere may be limited to the undetectable cloud particles. Additional direct and indirect measurements of the chemical and microphysical characteristics of overshooting convection are required to validate the results of this study and to provide sufficient detail for identification of dominant pathways for convective injection into the lower stratosphere.

REFERENCES

Adler, R. F., M. J. Markus, D. D. Fenn, G. Szejwach, and W. E. Shenk, 1983: Thunderstorm top structure observed by aircraft overflights with an infrared radiometer. *J. Climate Appl. Meteor.,* **22,** 579–593, doi:10.1175/1520-0450(1983)022<0579:TTSOBA>2.0.CO;2.

Anderson, J. G., D. M. Wilmouth, J. B. Smith, and D. S. Sayres, 2012: UV dosage levels in summer: Increased risk of ozone loss from convectively injected water vapor. *Science,* **337,** 835–839, doi:10.1126/science.1222978.

Aydin, K., and T. A. Seliga, 1984: Radar polarimetric backscattering properties of conical graupel. *J. Atmos. Sci.,* **41,** 1887–1892, doi:10.1175/1520-0469(1984)041<1887:RPBPOC>2.0.CO;2.

Balakrishnan, N., and D. S. Zrnić, 1990: Use of polarization to characterize precipitation and discriminate large hail. *J. Atmos. Sci.,* **47,** 1525–1540, doi:10.1175/1520-0469(1990)047<1525:UOPTCP>2.0.CO;2.

Bedka, K. M., 2011: Overshooting cloud top detections using MSG SEVIRI infrared brightness temperatures and their relationship to severe weather over Europe. *Atmos. Res.,* **99,** 175–189, doi:10.1016/j.atmosres.2010.10.001.

——, J. Brunner, R. Dworak, W. Feltz, J. Otkin, and T. Greenwald, 2010: Objective satellite-based detection of overshooting tops using infrared window channel brightness temperature gradients. *J. Appl. Meteor. Climatol.,* **49,** 181–202, doi:10.1175/2009JAMC2286.1.

——, R. Dworak, J. Brunner, and W. Feltz, 2012: Validation of satellite-based objective overshooting cloud-top detection methods using CloudSat cloud profiling radar observations. *J. Appl. Meteor. Climatol.,* **51,** 1811–1822, doi:10.1175/JAMC-D-11-0131.1.

Berdeklis, P., and R. List, 2001: The ice crystal–graupel collision charging mechanism of thunderstorm electrification. *J. Atmos. Sci.,* **58,** 2751–2770, doi:10.1175/1520-0469(2001)058<2751: TICGCC>2.0.CO;2.

Borowska, L., D. Zrnić, A. Ryzhkov, P. Zhang, and C. Simmer, 2011: Polarimetric estimates of a 1-month accumulation of light rain with a 3-cm wavelength radar. *J. Hydrometeor.,* **12,** 1024–1039, doi:10.1175/2011JHM1339.1.

Bringi, V. N., and V. Chandrasekar, 2001: *Polarimetric Doppler Weather Radar.* Cambridge University Press, 636 pp.

Brunner, J. C., S. A. Ackerman, A. S. Bachmeier, and R. M. Rabin, 2007: A quantitative analysis of the enhanced-V feature in relation to severe weather. *Wea. Forecasting,* **22,** 853–872, doi:10.1175/WAF1022.1.

Calhoun, K. M., D. R. MacGorman, C. L. Ziegler, and M. I. Biggerstaff, 2013: Evolution of lightning activity and storm charge relative to dual-doppler analysis of a high-precipitation supercell storm. *Mon. Wea. Rev.,* **141,** 2199–2223, doi:10.1175/ MWR-D-12-00258.1.

Caylor, I. J., and V. Chandrasekar, 1996: Time-varying ice crystal orientation in thunderstorms observed with multiparameter radar. *IEEE Trans. Geosci. Remote Sens.,* **34,** 847–858, doi:10.1109/36.508402.

Connolly, P. J., C. P. R. Saunders, M. W. Gallagher, K. N. Bower, M. J. Flynn, T. W. Choularton, J. Whiteway, and R. P. Lawson, 2005: Aircraft observations of the influence of electric fields on the aggregation of ice crystals. *Quart. J. Roy. Meteor. Soc.,* **131,** 1695–1712, doi:10.1256/qj.03.217.

Crum, T. D., and R. L. Alberty, 1993: The WSR-88D and the WSR-88D operational support facility. *Bull. Amer. Meteor. Soc.,* **74,** 1669–1687, doi:10.1175/1520-0477(1993)074<1669: TWATWO>2.0.CO;2.

Cunningham, J. G., W. D. Zittel, R. R. Lee, and R. L. Ice, 2013: Methods for identifying systematic differential reflectivity (Z_{DR}) biases on the operational WSR-88D network. *36th Conf. on Radar Meteorology,* Breckenridge, CO, Amer. Meteor. Soc., 9B.5. [Available online at https://ams.confex.com/ ams/36Radar/webprogram/Paper228792.html.]

Deierling, W., and W. A. Petersen, 2008: Total lightning activity as an indicator of updraft characteristics. *J. Geophys. Res.,* **113,** D16210, doi:10.1029/2007JD009598.

——, ——, J. Latham, S. Ellis, and H. J. Christian, 2008: The relationship between lightning activity and ice fluxes in thunderstorms. *J. Geophys. Res.,* **113,** D15210, doi:10.1029/ 2007JD009700.

Dessler, A. E., and S. C. Sherwood, 2004: Effect of convection on the summertime extratropical lower stratosphere. *J. Geophys. Res.,* **109,** D23301, doi:10.1029/2004JD005209.

Dolan, B., and S. A. Rutledge, 2010: Using CASA IP1 to diagnose kinematic and microphysical interactions in a convective storm. *Mon. Wea. Rev.,* **138,** 1613–1634, doi:10.1175/2009MWR3016.1.

Doviak, R. J., and D. S. Zrnić, 1993: *Doppler Radar and Weather Observations.* 2nd ed. Dover Publications, 562 pp.

——, ——, J. Carter, A. Ryzhkov, S. Torres, and A. Zahrai, 1998: NOAA/NSSL's WSR-88D radar for research and enhancement of operations: Polarimetric upgrades to improve rainfall measurements. NSSL Tech. Rep. 110 pp. [Available online at http://www.nssl.noaa.gov/publications/wsr88d_reports/2pol_ upgrades.pdf.]

Dworak, R., K. Bedka, J. Brunner, and W. Feltz, 2012: Comparison between GOES-12 overshooting-top detections, WSR-88D radar reflectivity, and severe storm reports. *Wea. Forecasting,* **27,** 684–699, doi:10.1175/WAF-D-11-00070.1.

Feng, Z., X. Dong, B. Xi, C. Schumacher, P. Minnis, and M. Khaiyer, 2011: Top-of-atmosphere radiation budget of convective core/stratiform rain and anvil clouds from deep convective systems. *J. Geophys. Res.,* **116,** D23202, doi:10.1029/ 2011JD016451.

Fischer, H., and Coauthors, 2003: Deep convective injection of boundary layer air into the lowermost stratosphere at midlatitudes. *Atmos. Chem. Phys.,* **3,** 739–745, doi:10.5194/acp-3-739-2003.

Forster, P. M. F., and K. P. Shine, 1999: Stratospheric water vapour changes as a possible contributor to observed stratospheric cooling. *Geophys. Res. Lett.,* **26,** 3309–3312, doi:10.1029/ 1999GL010487.

Fujita, T. T., 1982: Principle of stereoscopic height computations and their applications to stratospheric cirrus over severe thunderstorms. *J. Meteor. Soc. Japan,* **60,** 355–368.

Gayet, J.-F., and Coauthors, 2012: On the observation of unusual high concentration of small chain-like aggregate ice crystals and large ice water contents near the top of a deep convective cloud during the CIRCLE-2 experiment. *Atmos. Chem. Phys.,* **12,** 727–744, doi:10.5194/acp-12-727-2012.

Hanisco, T. F., and Coauthors, 2007: Observations of deep convective influence on stratospheric water vapor and its isotopic composition. *Geophys. Res. Lett.,* **34,** L04814, doi:10.1029/ 2006GL027899.

Hegglin, M. I., and Coauthors, 2004: Tracing troposphere-to-stratosphere transport above a mid-latitude deep convective system. *Atmos. Chem. Phys.,* **4,** 741–756, doi:10.5194/acp-4-741-2004.

Herzegh, P. H., and R. E. Carbone, 1984: The influence of antenna illumination function characteristics on differential reflectivity measurements. *Preprints, 22nd Conf. on Radar Meteorology,* Zurich, Switzerland, Amer. Meteor. Soc., 281–286.

——, and A. R. Jameson, 1992: Observing precipitation through dual-polarization radar measurements. *Bull. Amer. Meteor. Soc.,* **73,** 1365–1374, doi:10.1175/1520-0477(1992)073<1365: OPTDPR>2.0.CO;2.

Homeyer, C. R., 2014: Formation of the enhanced-V infrared cloud-top feature from high-resolution three-dimensional radar observations. *J. Atmos. Sci.,* **71,** 332–348, doi:10.1175/JAS-D-13-079.1.

——, K. P. Bowman, and L. L. Pan, 2010: Extratropical tropopause transition layer characteristics from high-resolution sounding data. *J. Geophys. Res.,* **115,** D13108, doi:10.1029/2009JD013664.

——, L. L. Pan, and M. C. Barth, 2014a: Transport from convective overshooting of the extratropical tropopause and the role of large-scale lower stratosphere stability. *J. Geophys. Res. Atmos.,* **119,** 2220–2240, doi:10.1002/2013JD020931.

——, and Coauthors, 2014b: Convective transport of water vapor into the lower stratosphere observed during double-tropopause events. *J. Geophys. Res. Atmos.,* **119,** 10 941–10 958, doi:10.1002/ 2014JD021485.

Hubbert, J. C., V. N. Bringi, L. D. Carey, and S. Bolen, 1998: CSU-CHILL polarimetric radar measurements from a severe hail storm in eastern Colorado. *J. Appl. Meteor.,* **37,** 749–775, doi:10.1175/1520-0450(1998)037<0749:CCPRMF>2.0.CO;2.

——, ——, and D. Brunkow, 2003: Studies of the polarimetric covariance matrix. Part I: Calibration methodology. *J. Atmos. Oceanic Technol.,* **20,** 696–706, doi:10.1175/ 1520-0426(2003)20<696:SOTPCM>2.0.CO;2.

Knight, C. A., and N. C. Knight, 1973: Conical graupel. *J. Atmos. Sci.,* **30,** 118–124, doi:10.1175/1520-0469(1973)030<0118:CG>2.0.CO;2.

Kumjian, M. R., 2013a: Principles and applications of dual-polarization weather radar. Part I: Description of the polarimetric radar variables. *J. Oper. Meteor.,* **1,** 226–242, doi:10.15191/ nwajom.2013.0119.

——, 2013b: Principles and applications of dual-polarization weather radar. Part II: Warm and cold season applications. *J. Oper. Meteor.,* **1,** 243–264, doi:10.15191/nwajom.2013.0120.

——, 2013c: Principles and applications of dual-polarimetric weather radar. Part III: Artifacts. *J. Oper. Meteor.,* **1,** 265–274, doi:10.15191/nwajom.2013.0121.

——, and A. V. Ryzhkov, 2008: Polarimetric signatures in supercell thunderstorms. *J. Appl. Meteor. Climatol.,* **47,** 1940–1961, doi:10.1175/2007JAMC1874.1.

——, and ——, 2012: The impact of size sorting on the polarimetric radar variables. *J. Atmos. Sci.,* **69,** 2042–2060, doi:10.1175/JAS-D-11-0125.1.

——, A. P. Khain, N. Benmoshe, E. Ilotoviz, A. V. Ryzhkov, and V. T. J. Phillips, 2014: The anatomy and physics of Z_{DR} columns: Investigating a polarimetric radar signature with a spectral bin microphysical model. *J. Appl. Meteor. Climatol.,* **53,** 1820–1843, doi:10.1175/JAMC-D-13-0354.1.

Lane, T. P., and R. D. Sharman, 2006: Gravity wave breaking, secondary wave generation, and mixing above deep convection in a three-dimensional cloud model. *Geophys. Res. Lett.,* **33,** L23813, doi:10.1029/2006GL027988.

——, ——, T. L. Clark, and H.-M. Hsu, 2003: An investigation of turbulence generation mechanisms above deep convection. *J. Atmos. Sci.,* **60,** 1297–1321, doi:10.1175/1520-0469(2003)60<1297:AIOTGM>2.0.CO;2.

Lang, T. J., and S. A. Rutledge, 2008: Kinematic, microphysical, and electrical aspects of an asymmetric bow-echo mesoscale convective system observed during STEPS 2000. *J. Geophys. Res.,* **113,** D08213, doi:10.1029/2006JD007709.

Langston, C., J. Zhang, and K. Howard, 2007: Four-dimensional dynamic radar mosaic. *J. Atmos. Oceanic Technol.,* **24,** 776–790, doi:10.1175/JTECH2001.1.

Levizzani, V., and M. Setvák, 1996: Multispectral, high-resolution satellite observations of plumes on top of convective storms. *J. Atmos. Sci.,* **53,** 361–369, doi:10.1175/1520-0469(1996)053<0361:MHRSOO>2.0.CO;2.

Luderer, G., J. Trentmann, K. Hungershöfer, M. Herzog, M. Fromm, and M. O. Andreae, 2007: Small-scale mixing processes enhancing troposphere-to-stratosphere transport by pyro-cumulonimbus storms. *Atmos. Chem. Phys.,* **7,** 5945–5957, doi:10.5194/acp-7-5945-2007.

McCann, D. W., 1983: The enhanced-V: A satellite observable severe storm signature. *Mon. Wea. Rev.,* **111,** 887–894, doi:10.1175/1520-0493(1983)111<0887:TEVASO>2.0.CO;2.

Melnikov, V. M., D. S. Zrnić, R. J. Doviak, and J. K. Carter, 2003: Calibration and performance analysis of NSSL's polarimetric WSR-88D. NSSL Tech Rep., 77 pp. [Available online at http://www.nssl.noaa.gov/publications/wsr88d_reports/Calibration_and_Performance_Analysis.pdf.]

——, R. J. Doviak, D. S. Zrnić, and D. J. Stensrud, 2011: Mapping Bragg scatter with a polarimetric WSR-88D. *J. Atmos. Oceanic Technol.,* **28,** 1273–1285, doi:10.1175/JTECH-D-10-05048.1.

——, ——, ——, and ——, 2013a: Structures of Bragg scatter observed with the polarimetric WSR-88D. *J. Atmos. Oceanic Technol.,* **30,** 1253–1258, doi:10.1175/JTECH-D-12-00210.1.

——, D. S. Zrnić, M. Schmidt, and R. Murnan, 2013b: Z_{DR} calibration issues in the WSR-88Ds. NSSL. Tech. Rep., 55 pp. [Available online at http://www.nssl.noaa.gov/publications/wsr88d_reports/WSR88D_ZDRcalib_Report_2013.pdf.]

Mullendore, G. L., D. R. Durran, and J. R. Holton, 2005: Cross-tropopause tracer transport in midlatitude convection. *J. Geophys. Res.,* **110,** D06113, doi:10.1029/2004JD005059.

Musil, D. J., A. J. Heymsfield, and P. L. Smith, 1986: Microphysical characteristics of a well-developed weak echo region in a high plains supercell thunderstorm. *J. Climate Appl. Meteor.,* **25,** 1037–1051, doi:10.1175/1520-0450(1986)025<1037:MCOAWD>2.0.CO;2.

Negri, A. J., 1982: Cloud-top structure of tornadic storms on 10 April 1979 from rapid scan and stereo satellite observations. *Bull. Amer. Meteor. Soc.,* **63,** 1151–1159.

Pointin, Y., D. Ramond, and J. Fournet-Fayard, 1988: Radar differential reflectivity Z_{DR}: A real-case evaluation of errors induced by antenna characteristics. *J. Atmos. Oceanic Technol.,* **5,** 416–423, doi:10.1175/1520-0426(1988)005<0416:RDRARC>2.0.CO;2.

Ray, E. A., and Coauthors, 2004: Evidence of the effect of summertime midlatitude convection on the subtropical lower stratosphere from CRYSTAL-FACE tracer measurements. *J. Geophys. Res.,* **109,** D18304, doi:10.1029/2004JD004655.

Rowe, A. K., S. A. Rutledge, and T. J. Lang, 2011: Investigation of microphysical processes occurring in isolated convection during NAME. *Mon. Wea. Rev.,* **139,** 424–443, doi:10.1175/2010MWR3494.1.

——, ——, and ——, 2012: Investigation of microphysical processes occurring in organized convection during NAME. *Mon. Wea. Rev.,* **140,** 2168–2187, doi:10.1175/MWR-D-11-00124.1.

Ryzhkov, A. V., 2007: The impact of beam broadening on the quality of radar polarimetric data. *J. Atmos. Oceanic Technol.,* **24,** 729–744, doi:10.1175/JTECH2003.1.

——, and D. S. Zrnić, 2007: Depolarization in ice crystals and its effect on radar polarimetric measurements. *J. Atmos. Oceanic Technol.,* **24,** 1256–1267, doi:10.1175/JTECH2034.1.

——, S. E. Giangrande, V. M. Melnikov, and T. J. Schuur, 2005a: Calibration issues of dual-polarization radar measurements. *J. Atmos. Oceanic Technol.,* **22,** 1138–1155, doi:10.1175/JTECH1772.1.

——, ——, and T. J. Schuur, 2005b: Rainfall estimation with a polarimetric prototype of WSR-88D. *J. Appl. Meteor.,* **44,** 502–515, doi:10.1175/JAM2213.1.

——, T. J. Schuur, D. W. Burgess, P. L. Heinselman, S. E. Giangrande, and D. S. Zrnić, 2005c: The Joint Polarization Experiment: Polarimetric rainfall measurements and hydrometeor classification. *Bull. Amer. Meteor. Soc.,* **86,** 809–824, doi:10.1175/BAMS-86-6-809.

——, M. R. Kumjian, S. M. Ganson, and P. Zhang, 2013: Polarimetric radar characteristics of melting hail. Part II: Practical implications. *J. Appl. Meteor. Climatol.,* **52,** 2871–2886, doi:10.1175/JAMC-D-13-074.1.

Schmetz, J., S. A. Tjemkes, M. Gube, and L. van de Berg, 1997: Monitoring deep convection and convective overshooting with METEOSAT. *Adv. Space Res.,* **19,** 433–441, doi:10.1016/S0273-1177(97)00051-3.

Setvák, M., and C. A. Doswell III, 1991: The AVHRR channel 3 cloud top reflectivity of convective storms. *Mon. Wea. Rev.,* **119,** 841–847, doi:10.1175/1520-0493(1991)119<0841:TACCTR>2.0.CO;2.

——, and Coauthors, 2010: Satellite-observed cold-ring-shaped features atop deep convective clouds. *Atmos. Res.,* **97,** 80–96, doi:10.1016/j.atmosres.2010.03.009.

——, K. Bedka, D. T. Lindsey, A. Sokol, Z. Charvát, J. Šťástka, and P. K. Wang, 2013: A-Train observations of deep convective storm tops. *Atmos. Res.,* **123,** 229–248, doi:10.1016/j.atmosres.2012.06.020.

Solomon, S., K. H. Rosenlof, R. W. Portmann, J. S. Daniel, S. M. Davis, T. J. Sanford, and G.-K. Plattner, 2010: Contributions of

stratospheric water vapor to decadal changes in the rate of global warming. *Science,* **327,** 1219–1223, doi:10.1126/science.1182488.

Stith, J. L., and Coauthors, 2014: Ice particles in the upper anvil regions of midlatitude continental thunderstorms: The case for frozen-drop aggregates. *Atmos. Chem. Phys.,* **14,** 1973–1985, doi:10.5194/acp-14-1973-2014.

Straka, J. M., D. S. Zrnić, and A. V. Ryzhkov, 2000: Bulk hydrometeor classification and quantification using polarimetric radar data: Synthesis of relations. *J. Appl. Meteor.,* **39,** 1341–1372, doi:10.1175/1520-0450(2000)039<1341:BHCAQU>2.0.CO;2.

Tessendorf, S. A., K. C. Wiens, and S. A. Rutledge, 2007: Radar and lightning observations of the 3 June 2000 electrically inverted storm from STEPS. *Mon. Wea. Rev.,* **135,** 3665–3681, doi:10.1175/2006MWR1953.1.

Trapp, R. J., and C. A. Doswell III, 2000: Radar data objective analysis. *J. Atmos. Oceanic Technol.,* **17,** 105–120, doi:10.1175/1520-0426(2000)017<0105:RDOA>2.0.CO;2.

Ventura, J. F. I., F. Honore, and P. Tabary, 2013: X-band polarimetric weather radar observations of a hailstorm. *J. Atmos. Oceanic Technol.,* **30,** 2143–2151, doi:10.1175/JTECH-D-12-00243.1.

Vivekanandan, J., D. S. Zrnić, S. M. Ellis, R. Oye, A. V. Ryzhkov, and J. Straka, 1999: Cloud microphysics retrieval using S-band dual-polarization radar measurements. *Bull. Amer. Meteor.*

Soc., **80,** 381–388, doi:10.1175/1520-0477(1999)080<0381: CMRUSB>2.0.CO;2.

Wang, P. K., 2003: Moisture plumes above thunderstorm anvils and their contributions to cross-tropopause transport of water vapor in midlatitudes. *J. Geophys. Res.,* **108,** 4194, doi:10.1029/2002JD002581.

Yuter, S. E., and R. A. Houze Jr., 1995: Three-dimensional kinematic and microphysical evolution of Florida cumulonimbus. Part II: Frequency distributions of vertical velocity, reflectivity, and differential reflectivity. *Mon. Wea. Rev.,* **123,** 1941–1963, doi:10.1175/1520-0493(1995)123<1941: TDKAME>2.0.CO;2.

Zhang, J., K. Howard, and J. J. Gourley, 2005: Constructing three-dimensional multiple-radar reflectivity mosaics: Examples of convective storms and stratiform rain echoes. *J. Atmos. Oceanic Technol.,* **22,** 30–42, doi:10.1175/JTECH-1689.1.

Zrnić, D. S., and A. V. Ryzhkov, 1999: Polarimetry for weather surveillance radars. *Bull. Amer. Meteor. Soc.,* **80,** 389–406, doi:10.1175/1520-0477(1999)080<0389:PFWSR>2.0.CO;2.

——, V. N. Bringi, N. Balakrishnan, K. Aydin, V. Chandrasekar, and J. Hubbert, 1993: Polarimetric measurements in a severe hailstorm. *Mon. Wea. Rev.,* **121,** 2223–2238, doi:10.1175/1520-0493(1993)121<2223:PMIASH>2.0.CO;2.